

CHEMICAL COMPOSITION OF TWO BRIGHT EXTREMELY METAL-POOR STARS FROM THE  
SDSS MARVELS PRE-SURVEYAVRAJIT BANDYOPADHYAY<sup>1</sup>, SIVARANI THIRUPATHI<sup>1</sup>, ANTONY SUSMITHA<sup>1</sup>, TIMOTHY C. BEERS<sup>2</sup>, SUNETRA GIRIDHAR<sup>1</sup>, ARUN  
SURYA<sup>1</sup>, THOMAS MASSERON<sup>3</sup>*Draft version May 8, 2018*

## Abstract

SDSS J082625.70+612515.10 ( $V = 11.4$ ;  $[\text{Fe}/\text{H}] = -3.1$ ) and SDSS J134144.60+474128.90 ( $V = 12.4$ ;  $[\text{Fe}/\text{H}] = -3.2$ ) were observed with the SDSS 2.5-m telescope as part of the SDSS-MARVELS spectroscopic pre-survey, and were identified as extremely metal-poor (EMP;  $[\text{Fe}/\text{H}] < -3.0$ ) stars during high-resolution follow-up with the Hanle Echelle Spectrograph (HESP) on the 2.3-m Himalayan Chandra Telescope. In this paper, the first science results using HESP, we present a detailed analysis of their chemical abundances. Both stars exhibit under-abundances in their neutron-capture elements, while one of them, SDSS J134144.60+474128.90, is clearly enhanced in carbon. Lithium was also detected in this star at a level of about  $A(\text{Li}) = 1.95$ . The spectra were obtained over a span of 6-24 months, and indicate that both stars could be members of binary systems. We compare the elemental abundances derived for these two stars along with other carbon-enhanced metal-poor (CEMP) and EMP stars, in order to understand the nature of their parent supernovae. We find that CEMP-no stars and EMP dwarfs exhibit very similar trends in their lithium abundances at various metallicities. We also find indications that CEMP-no stars have larger abundances of Cr and Co at a given metallicity, compared to EMP stars.

**Keywords:** stars: abundances — stars: carbon — stars: early-type — stars: neutron — stars: Population III

## 1. INTRODUCTION

Extremely metal-poor (EMP;  $[\text{Fe}/\text{H}] < -3.0$ ) stars of the Galactic halo are thought to be the immediate successors of the first stars, and were likely to have formed when the Universe was only a few hundred million years old (e.g., Bromm et al. 2009) – their evolution and explosion led to the first production of heavy elements. These first supernovae had a considerable dynamical, thermal, and chemical impact on the evolution of the surrounding interstellar medium, including mini-halos that can be some distance away from the location of the first-star explosion (Cooke & Madau 2014; Smith et al. 2015; Chiaki et al. 2018). Stars (and their host galaxies) that formed thereafter are expected to carry the imprints of the nucleosynthesis events from these Population III stars (Beers & Christlieb 2005; Frebel & Norris 2015; Sharma et al. 2018). Studies of such EMP stars have greatly benefited from the large spectroscopic surveys that were carried out in the past in order to identify them in significant numbers, such as the HK survey of Beers and collaborators (Beers et al. 1985, 1992) and the Hamburg/ESO Survey of Christlieb and colleagues (Christlieb 2003). More recent surveys, such as SDSS, RAVE, APOGEE and LAMOST continue to expand the known members of this rare class of stars (e.g., Fulbright et al. 2010; Ivezić et al. 2012; Aoki et al. 2013; Zhao et al. 2012; García Pérez et al. 2013; Anders et al. 2014; Li et al. 2015).

High-resolution spectroscopic studies of metal-poor Galactic halo stars have demonstrated diversity in their chemical compositions. For example, on the order of 20% of stars with  $[\text{Fe}/\text{H}] < -2.0$  exhibit large enhancements in their carbon-

to-iron ratios ( $[\text{C}/\text{Fe}] > +0.7$ ; Aoki et al. 2007; Lee et al. 2013; Lee et al. 2017). As shown by numerous studies, the frequency of carbon-enhanced metal-poor (CEMP) stars continues to increase with decreasing  $[\text{Fe}/\text{H}]$ . The fractions of CEMP stars also increase with distance from the Galactic plane (Frebel et al. 2006; Beers et al. 2017), and also between the inner-halo and the outer-halo regions (Lee et al. 2017).

CEMP stars can be separated into four sub-classes (Beers & Christlieb 2005): i) CEMP-*s* stars, which show enhancements of *s*-process elements, ii) CEMP-*r* stars, which exhibit enhancements of *r*-process elements, iii) CEMP-*r/s* stars, which show enhancements in both *r*- and *s*-process elements<sup>4</sup>, and iv) CEMP-no stars, which exhibit no neutron-capture element enhancements. Long-term radial-velocity monitoring studies have shown that most ( $> 80\%$ , possibly all) CEMP-*s* stars are members of binary systems involving a (now extinct) asymptotic giant branch (AGB) star that transferred carbon and *s*-process rich material to the presently observed (lower-mass) star (Lucatello et al. 2005; Starkenburg et al. 2014; Hansen et al. 2016b), while CEMP-no stars exhibit observed binary frequencies typical of non-carbon-enhanced halo giants,  $\sim 18\%$  (Starkenburg et al. 2014; Hansen et al. 2016a).

Yoon et al. (2016) have considered the rich morphology of the absolute abundance of carbon,  $A(\text{C}) = \log(C)$ , as a function of  $[\text{Fe}/\text{H}]$ , based on high-resolution analyses of a large sample of CEMP stars (their Figure 1, the Yoon-Beers diagram). In addition to their Group I stars, which are dominated by CEMP-*s* stars, they demonstrate that the CEMP-no stars not only exhibit substantially lower  $A(\text{C})$ , but bifurcate into two apparently different regions of the diagram, which they refer to as Group II and Group III stars. This behavior

avrajit@iia.res.in, sivarani@iia.res.in

<sup>1</sup> Indian Institute of Astrophysics, Bangalore<sup>2</sup> Department of Physics and JINA Center for the Evolution of the Elements, University of Notre Dame, Notre Dame, IN, 46656, USA<sup>3</sup> Departamento de Astrofísica, Universidad de La Laguna, E-38206 La Laguna, Tenerife, Spain<sup>4</sup> Hampel et al. (2016) suggest that the observed heavy element patterns of these stars are well accounted for by an “intermediate neutron-capture process,” (as first suggested by Cowan & Rose 1977), and should be referred to henceforth as CEMP-*i* stars.

immediately suggests that these groups might be associated with different progenitors responsible for the carbon production, a suggestion borne out by the modeling carried out by Placco et al. (2016), and/or on the masses of the mini-halos in which these stars formed. Chiaki et al. (2017) have emphasized that different cooling pathways, dependent on the formation of carbon or silicate dust, may have applied to the Group III and Group II stars in the Yoon-Beers diagram.

Multiple models for the production of CEMP-no stars have been considered in the literature, such as the “spin-star” models (e.g., Meynet et al. 2006; Meynet et al. 2010; Chiappini 2013), and the “mixing and fallback” models for faint SNe (e.g., Umeda & Nomoto 2003; Umeda & Nomoto 2005; Nomoto et al. 2013; Tominaga et al. 2014). Both processes may well play a role (Maeder & Meynet 2015; Choplin et al. 2016).

Regardless of the complexity of the situation, additional detailed observations of EMP stars with and without clear carbon enhancement, such as those carried out here, are required for progress in understanding. This paper is outlined as follows. In Section 2 we describe our high-resolution observations. Consideration of possible radial-velocity variations for our two targets is presented in Section 3. Section 4 summarizes our estimates of stellar atmospheric parameters, and describes our abundance analyses. Results of the abundance analysis are reported in Section 5. We present a discussion of our results with a comparative study of CEMP-no and EMP stars in Section 6, along with a brief conclusion in Section 7.

## 2. OBSERVATIONS AND ANALYSIS

### 2.1. Sample Selection

MARVELS (Paegert et al. 2015), a multi-object radial-velocity survey designed for efficient exo-planet searches, was one of the three sub-surveys carried out as part of SDSS-III (Eisenstein et al. 2011). The targets for the first two years of MARVELS were selected based on a lower-resolution ( $R \sim 1800$ ) spectroscopic pre-survey using the SDSS spectrographs. Most of the pre-survey observations were carried out during twilight, when the fields were at low elevation. Targets were selected from these pre-survey fields for the MARVELS main radial velocity (RV) survey, which were later observed at higher elevations. There were about 30,000 stars observed as part of the spectroscopic pre-survey of stars with  $B - V > 0.6$  and  $8 < V < 13$ . Target fields for the first two years of the MARVELS survey were around known RV standards, and about 75% of the target fields were in the Galactic latitude range  $2^\circ < |b| < 30^\circ$ . Although not the ideal location to find metal-poor stars, it does offer the chance to identify a small number of bright halo targets, suitable for high-resolution spectroscopic follow-up with moderate-aperture telescopes, that happen to fall into the MARVELS pre-survey footprint during their orbits about the Galactic center. The pre-survey also has simple magnitude and color cuts, which reduces potential selection biases. As in our previously published work (Susmitha Rani et al. 2016), we used synthetic spectral fitting of the pre-survey data to identify new metal-poor candidates. Here, we present high-resolution observations and analysis of two EMP stars, SDSS J082625.70+612515.10 (hereafter, SDSS J0826+6125) and SDSS J134144.60+474128.90 (hereafter, SDSS J1341+4741), with  $V$  magnitudes of 11.44 and 12.38, respectively. These two stars were selected for follow up, as they were found to be very metal poor from spectral

**Table 1**  
Observation log and radial velocities for SDSS J0826+6125

| Date       | MJD         | $\lambda$ Coverage<br>(Å) | SNR | Radial Velocity<br>(km sec <sup>-1</sup> ) |
|------------|-------------|---------------------------|-----|--|
| 2015-11-03 | 57330.20903 | 3600-10800                | 51  | -110.4                                     |
| 2015-11-29 | 57356.36042 | 3600-10800                | 49  | -95.6                                      |
| 2015-12-22 | 57379.10417 | 3600-10800                | 47  | -80.3                                      |
| 2016-01-27 | 57415.09792 | 3600-10800                | 47  | -52.3                                      |
| 2016-10-20 | 57682.21667 | 3600-10800                | 50  | -108.9                                     |
| 2016-11-16 | 57709.13542 | 3600-10800                | 51  | -104.1                                     |

**Table 2**  
Observation log and radial velocities for SDSS J1341+4741

| Date       | MJD         | $\lambda$ Coverage<br>(Å) | SNR | Radial Velocity<br>(km sec <sup>-1</sup> ) |
|------------|-------------|---------------------------|-----|--|
| 2016-27-01 | 57415.24722 | 3600-10800                | 43  | -240.1                                     |
| 2016-24-04 | 57503.18819 | 3600-10800                | 49  | -190.5                                     |
| 2016-26-04 | 57505.06458 | 3600-10800                | 47  | -192.1                                     |
| 2016-24-06 | 57564.02361 | 3600-10800                | 48  | -176.2                                     |
| 2016-25-06 | 57565.20139 | 3600-10800                | 47  | -174.5                                     |

fitting of the pre-survey data, and were also very bright. Results from the spectral fitting used to identify metal-poor candidates from the MARVELS pre-survey will be discussed in a separate paper.

### 2.2. High-Resolution Observations

High-resolution ( $R \sim 30,000$ ) spectroscopic observations of the two EMP stars were obtained with the Hanle Echelle Spectrograph (HESP) on the 2.3-m Himalayan Chandra telescope (HCT) at the Indian Astronomical Observatory (IAO). The dates of observation, wavelength coverage, radial velocities, and signal-to-noise ratios of the available spectra are listed in Tables 1 and 2.

Data reduction was carried out using the IRAF<sup>5</sup> echelle package. HESP has a dual fiber mode available, one fiber for the target star and another, which can be fed with a calibration source for precise RV measurements, or by the night sky through a pinhole that has a separation of about  $13''$  from the target. The sky fiber is used for background subtraction. All the orders were normalized, corrected for radial velocity, and merged to produce the final spectrum. The equivalent widths for individual species are listed in the tables in the appendix. Recently, a custom data reduction pipeline has been developed by A. Surya (available publicly<sup>6</sup>) that is more suitable for the crowded and curved orders of the stellar spectra observed with HESP. However, in the present paper, we use IRAF, and proper care was taken to avoid drift of the spectral tracings blending into adjacent orders.

## 3. RADIAL VELOCITIES

The HESP instrument is thermally controlled to  $\Delta T = \pm 0.1^\circ \text{C}$  at a set point of  $16^\circ \text{C}$  over the entire year, which is expected to provide a long-term stability of  $\sim 200 \text{ m s}^{-1}$  (Sivarani et al. in preparation), substantially lowering systematic errors with respect to a spectrograph that does not have such control.

<sup>5</sup> IRAF is distributed by the National Optical Astronomy Observatory, which is operated by the Association of Universities for Research in Astronomy (AURA) under cooperative agreement with the National Science Foundation.

<sup>6</sup> <https://www.iiaa.res.in/hesp/>

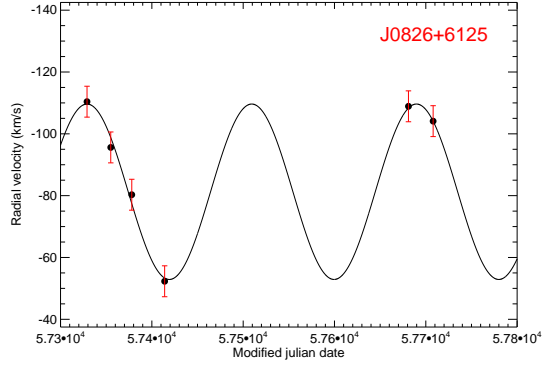


**Figure 1.** Variation of radial velocity for SDSS J0826+6125. The derived period is of 180.4 days

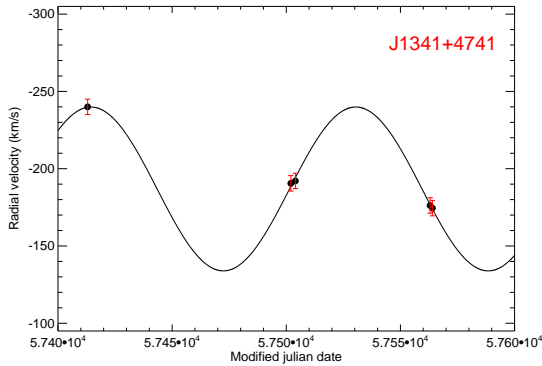


**Figure 2.** Variation of radial velocity for SDSS J1341+4741. The derived period is 116.0 days

RVs were calculated for SDSS J0826+6125 based on six epochs of observations spread over a period of 12 months. For SDSS J1341+4741, we obtained five observations spread over six months. A cross-correlation analysis was performed with a synthetic template spectrum suitable for each star to obtain the RV measurement for each spectrum. We made use of the software package RVLIN provided by Wright & Howard (2009), which is a set of IDL routines used to fit Keplerian orbits to derive the orbital parameters from the RV data. The RV measurements exhibit peak-to-peak variations of  $\sim 60 \text{ km s}^{-1}$ , with a period of 180 days for SDSS J0826+6125, and  $\sim 110 \text{ km s}^{-1}$ , with a period of 116 days for SDSS J1341+4741. The best-fit orbits for these stars, based on the data in hand, are shown in Figures 1 and 2. Although the existence of RV variations is secure, with such sparse coverage of the proposed orbits more data are required to confirm the periods.

#### 4. STELLAR PARAMETERS

Both photometric and spectroscopic data were used to derive estimates of the stellar parameters for our program stars. The effective temperatures were determined using various photometric observations in the literature and the  $T_{\text{eff}}$ -color relations derived by Ramírez & Meléndez (2005). They were found to be in close proximity (a difference of 40 K was found) to values obtained using Alonso et al. (1996) and Alonso et al. (1999). The  $V - K$  temperature estimate is expected to be superior, as it is least affected by metallicity and the possible presence of molecular carbon bands. We also em-

**Table 3**  
Estimates of Effective Temperature

| Method     | $T_{\text{eff}}$ (K) |                 |
|------------|----------------------|-----------------|
|            | SDSS J0826+6125      | SDSS J1341+4741 |
| $V - K$    | 4453                 | 5827            |
| SED        | 4500                 | 5500            |
| $H\alpha$  | 4400                 | 5450            |
| Fe I/Fe II | 4300                 | 5400            |

**Table 4**  
Adopted Stellar Parameters

| Object          | $T_{\text{eff}}$ (K) | $\log(g)$ | $\xi$ | [Fe/H] |
|-----------------|----------------------|-----------|-------|--------|
| SDSS J0826+6125 | 4300                 | 0.40      | 1.80  | -3.10  |
| SDSS J1341+4741 | 5450                 | 2.50      | 1.80  | -3.20  |

ployed VOSA (<http://svo2.cab.inta-csic.es/>), the online SED fitter (Bayo et al. 2008), to derive the temperatures using all of the available photometry (optical, 2MASS, and WISE). A Bayesian fit using the Kurucz ODFNEW/NOVER model was used to obtain the SED temperature. Final fits for the two stars are shown in Figures 3 and 4.

$T_{\text{eff}}$  estimates have also been derived spectroscopically, by demanding that there be no trend of Fe I line abundances with excitation potential (shown in the upper panels of Figures 5 and 6), as well by fitting the  $H\alpha$  profiles. Estimates for the effective temperatures of our target stars are listed in Table 3. For SDSS J1341+4741, we have adopted the temperature obtained from fitting of the  $H\alpha$  wings, as it is highly sensitive to small variations in temperature. For SDSS J0826+6125, the  $H\alpha$  profile was asymmetric, and thus it could not be used for accurate measurement of temperature. So, the temperature obtained from Fe I line abundances was adopted.

Surface gravity,  $\log(g)$ , estimates for the two stars have been determined by the usual technique that demands equality of the iron abundances derived for the neutral (Fe I) lines and singly ionized (Fe II) lines. We used 7 Fe II lines and 82 Fe I lines for SDSS J0826+6125, and 5 Fe II lines and 49 Fe I lines for SDSS J1341+4741; best-fit models for our target stars are shown in the upper panels of Figures 5 and 6. The wings of the Mg I lines have also been fitted to obtain estimates for  $\log(g)$ ; best-fit models are shown in Figure 7.

The microturbulent velocity ( $\xi$ ) estimates for each star have been derived iteratively in this process, by demanding no trend of Fe I abundances with the reduced equivalent widths, and are plotted in the lower panels of figures 5 and 6. The final adopted stellar atmospheric parameters are listed in Table 4.

#### 4.1. Abundance Analysis

To determine the abundance estimates for the various elements present in our target stars we have employed one dimensional LTE stellar atmospheric models (ATLAS9; Castelli & Kurucz 2004) and the spectral synthesis code turbospectrum (Alvarez & Plez 1998). We measured the equivalent widths of the absorption lines present in the spectra, and considered only those lines for abundance analysis whose equivalent width is less than 120 mÅ, since they are on the linear part of the curve of growth, and are relatively insensitive to the choice of microturbulence. We measured the equivalent widths of 53 clean lines present in the spectra of SDSS J0826+6125, among which 82 are Fe I lines, and 122 clean lines for SDSS J1341+4741, among which 49 are

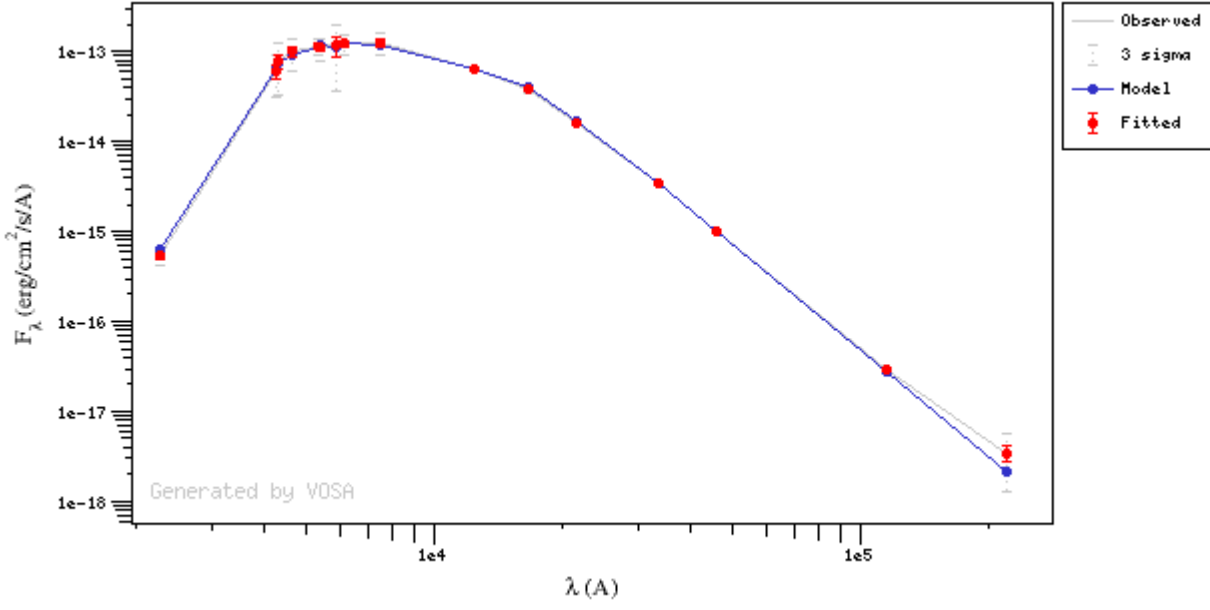


**Figure 3.** The SED obtained from VOSA for SDSS J0826+6125 shows the temperature to be  $\sim 4500$  K.

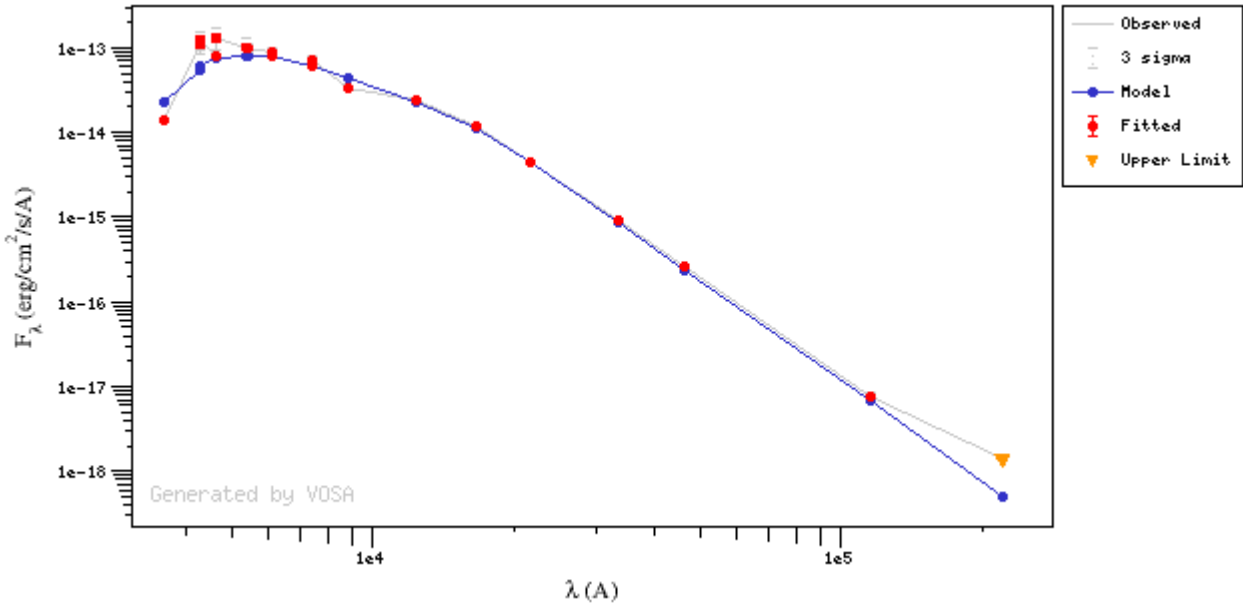


**Figure 4.** The SED obtained from VOSA for SDSS J1341+4741 shows the temperature to be  $\sim 5500$  K.

**Table 5**  
Elemental Abundance Determinations for SDSS J0826+6125

| Elements        | Species | $N_{lines}$ | A(X)  | Solar | [X/H] | [X/Fe]             | $\sigma^*$ |
|-----------------|---------|-------------|-------|-------|-------|--------------------|------------|
| C <sup>s</sup>  | CH      | ...         | 4.60  | 8.43  | -3.92 | -0.82              | 0.04       |
| N <sup>s</sup>  | CN      | ...         | 6.00  | 7.83  | -1.83 | +1.27              | 0.03       |
| O <sup>s</sup>  | O I     | ...         | 6.50  | 8.69  | -2.19 | +0.91              | 0.01       |
| Na <sup>s</sup> | Na I    | 2           | 3.30  | 6.21  | -2.91 | +0.19 <sup>b</sup> | 0.01       |
| Mg <sup>s</sup> | Mg I    | 4           | 5.05  | 7.59  | -2.54 | +0.56              | 0.01       |
| Al <sup>s</sup> | Al I    | 1           | 3.40  | 6.43  | -3.03 | +0.07 <sup>b</sup> | 0.02       |
| Ca              | Ca I    | 8           | 3.68  | 6.32  | -2.64 | +0.46              | 0.06       |
| Sc <sup>s</sup> | Sc II   | 5           | -0.06 | 3.15  | -3.21 | -0.11              | 0.01       |
| Ti              | Ti I    | 7           | 1.96  | 4.93  | -2.97 | +0.13              | 0.03       |
|                 | Ti II   | 6           | 2.06  | 4.93  | -2.87 | +0.23              | 0.04       |
| Cr              | Cr I    | 3           | 2.10  | 5.62  | -3.52 | -0.42              | 0.05       |
|                 | Cr II   | 2           | 2.35  | 5.62  | -3.27 | -0.17              | 0.05       |
| Mn <sup>s</sup> | Mn I    | 4           | 1.60  | 5.42  | -3.82 | -0.72              | 0.02       |
| Co <sup>s</sup> | Co I    | 2           | 2.00  | 4.93  | -2.93 | +0.17              | 0.01       |
| Ni              | Ni I    | 3           | 3.00  | 6.20  | -3.20 | -0.10              | 0.04       |
| Zn              | Zn I    | 2           | 1.50  | 4.56  | -2.96 | +0.14              | 0.05       |
| Sr <sup>s</sup> | Sr II   | 2           | -0.90 | 2.83  | -3.73 | -0.63              | 0.01       |
| Y <sup>s</sup>  | Y II    | 1           | -1.47 | 2.21  | -3.68 | -0.58              | 0.01       |
| Zr <sup>s</sup> | Zr II   | 2           | -0.75 | 2.59  | -3.34 | -0.24              | 0.01       |
| Ba <sup>s</sup> | Ba II   | 2           | -1.80 | 2.25  | -4.05 | -0.95              | 0.01       |

$\sigma^*$  indicates the error.

<sup>b</sup> Values obtained after applying NLTE corrections.

<sup>s</sup> Indicates abundances obtained using synthesis.

**Table 6**  
Elemental Abundance Determinations for SDSS J1341+4741

| Elements        | Species | $N_{lines}$ | A(X)  | Solar | [X/H] | [X/Fe]             | $\sigma^*$ |
|-----------------|---------|-------------|-------|-------|-------|--------------------|------------|
| Li <sup>s</sup> | Li I    | 1           | 1.95  | ...   | ...   | ...                | 0.01       |
| C <sup>s</sup>  | CH      | ...         | 6.22  | 8.43  | -2.21 | +0.99              | 0.04       |
| N <sup>s†</sup> | CN      | ...         | 7.00  | 7.83  | -0.83 | +2.37              | 0.05       |
| Na <sup>s</sup> | Na I    | 2           | 2.80  | 6.21  | -3.41 | -0.21 <sup>b</sup> | 0.01       |
| Mg <sup>s</sup> | Mg I    | 5           | 5.10  | 7.59  | -2.49 | +0.71              | 0.01       |
| Al <sup>b</sup> | Al I    | 1           | 3.2   | 6.43  | -3.23 | -0.03 <sup>b</sup> | 0.02       |
| Si              | Si I    | 1           | 5.33  | 7.51  | -2.18 | +1.02              | 0.07       |
| Ca              | Ca I    | 11          | 3.60  | 6.32  | -2.72 | +0.48              | 0.05       |
| Sc <sup>s</sup> | Sc II   | 3           | -0.1  | 3.16  | -3.26 | -0.06              | 0.01       |
| Ti              | Ti I    | 4           | 2.23  | 4.93  | -2.70 | +0.50              | 0.05       |
|                 | Ti II   | 13          | 1.89  | 4.93  | -3.04 | +0.16              | 0.04       |
| Cr              | Cr I    | 6           | 2.31  | 5.62  | -3.31 | -0.11              | 0.04       |
|                 | Cr II   | 1           | 2.77  | 5.62  | -2.85 | +0.35              | 0.06       |
| Mn              | Mn I    | 5           | 1.89  | 5.42  | -3.53 | -0.33              | 0.05       |
| Co              | Co I    | 2           | 1.99  | 4.93  | -2.96 | +0.24              | 0.05       |
| Ni              | Ni I    | 4           | 3.35  | 6.20  | -2.85 | +0.35              | 0.04       |
| Sr <sup>s</sup> | Sr II   | 2           | -0.88 | 2.83  | -3.71 | -0.51              | 0.01       |
| Ba <sup>s</sup> | Ba II   | 2           | -1.68 | 2.25  | -3.93 | -0.73              | 0.01       |

<sup>†</sup>Only upper limits could be derived.

$\sigma^*$  indicates the error.

<sup>b</sup> Values obtained after applying NLTE corrections.

<sup>s</sup> Indicates abundances obtained using synthesis

Fe I lines. We have adopted the solar abundances for each element from Asplund et al. (2009); Scott et al. (2015a,b); Grevesse et al. (2015); solar isotopic fractions were used for all the elements. Version 12 of the turbospectrum code for spectrum synthesis and abundance estimates have been used for the analysis. We have adopted the hyperfine splitting provided by McWilliam (1998) and solar isotopic ratios. We have also used 2D MARCS models (Gustafsson et al. 2008) to derive the abundances, but no significant deviations were obtained. The abundances differed by a values ranging from 0.01 to 0.02 dex for individual species.

## 5. ABUNDANCES

### 5.1. Carbon, Nitrogen, and Oxygen

Carbon-abundance estimates for our stars were derived by iteratively fitting the CH bandhead region with synthetic spec-

tra, and adopting the value that yields the best match. We have used the CH molecular line list compiled by Bertrand Plez (Plez & Cohen 2005). The CN and CH molecular linelists are taken from the Kurucz database.

For SDSS J0826+6125, the O I at 630 nm was used to measure the oxygen abundance, which was found to be strongly enhanced,  $[O/Fe] = +0.91$ . The chemical equilibrium of CO is taken into consideration in the turbospectrum synthesis code (de Laverny et al. 2012). We also have CO spectra, and though noisy, its oxygen abundance is consistent with the estimates from O I. The carbon abundance was obtained from the CH *G*-band region, which yielded a value of  $[C/Fe] = -0.82$ . We have also checked the sensitivity of the CH band for various O abundances, but no variation could be detected. The C<sub>2</sub> molecular band at 516.5 nm also could not be detected, which is consistent with a low C abundance. We could also detect the bandhead in the region of the CN band at 3884 Å, and obtain an enhancement in nitrogen corresponding to a value of  $[N/Fe] = +1.27$ .

For SDSS J1341+4741, the derived fit to the CH *G*-band yielded  $[C/Fe] = +0.99$ , clear evidence for its enhancement. Using medium-resolution spectroscopy from SDSS, Fernández-Alvar et al. (2016) has previously reported a carbon abundance ratio of  $[C/Fe] = +0.95$ . The O I line at 630 nm is too weak to be detected, hence no meaningful O abundance could be derived for this star. The signal-to-noise ratio at the region of CN band is too low to confirm enhancement in nitrogen for this star; so we could only obtain an upper limit of  $[N/Fe] < +2.37$ .

Fits for in the region of the CH *G*-band are shown for both stars in Figure 8.

### 5.2. The $\alpha$ -Elements

Several magnesium lines were detected in the spectra of our target stars. Two of the lines in the Mg triplet at 5172 Å, and three other lines at 4167 Å, 4702 Å, and 5528 Å, were used to obtain the abundances. The derived  $[Mg/Fe]$  ratios for SDSS J0826+6125 and SDSS J1341+4741 are  $[Mg/Fe] = +0.56$  and  $[Mg/Fe] = +0.71$ , respectively, values often found among halo stars. The silicon lines at 5268 Å and 6237 Å were too weak to be used for abundance estimates of SDSS J0826+6125, but for SDSS J1341+4741, we obtain  $[Si/Fe] = +1.0$ . It should be noted that Si may appear overabundant for metal-poor stars because LTE results are known to overestimate the true value (Shi et al. 2012).

Eight and eleven Ca I lines were detected in the spectra of SDSS J0826+6125 and SDSS J1341+4741, respectively, including the prominent lines at 4226.73 Å, 4302.53 Å, and 4454.78 Å, and used to measured its abundance. The measurements indicate slightly enhanced ratios of  $[Ca/Fe] = +0.46$  (for SDSS J0826+6125) and  $[Ca/Fe] = +0.48$  (for SDSS J1341+4741). The overall abundance of the  $\alpha$ -elements is consistent with the typical halo enhancement of  $[\alpha/Fe] = +0.4$ .

### 5.3. The Odd-Z Elements

The sodium abundance is determined from the Na *D*<sub>1</sub> and *D*<sub>2</sub> resonance lines at 5890 Å and 5896 Å. The aluminium abundance is obtained from one of the resonance lines at 3961.5 Å. This line is not the ideal indicator, as it can have large departures from LTE, as discussed by Baumüller & Gehren (1997), who found it to be as large as +0.6 dex. Gratton et al. (2001) showed that incorporation of

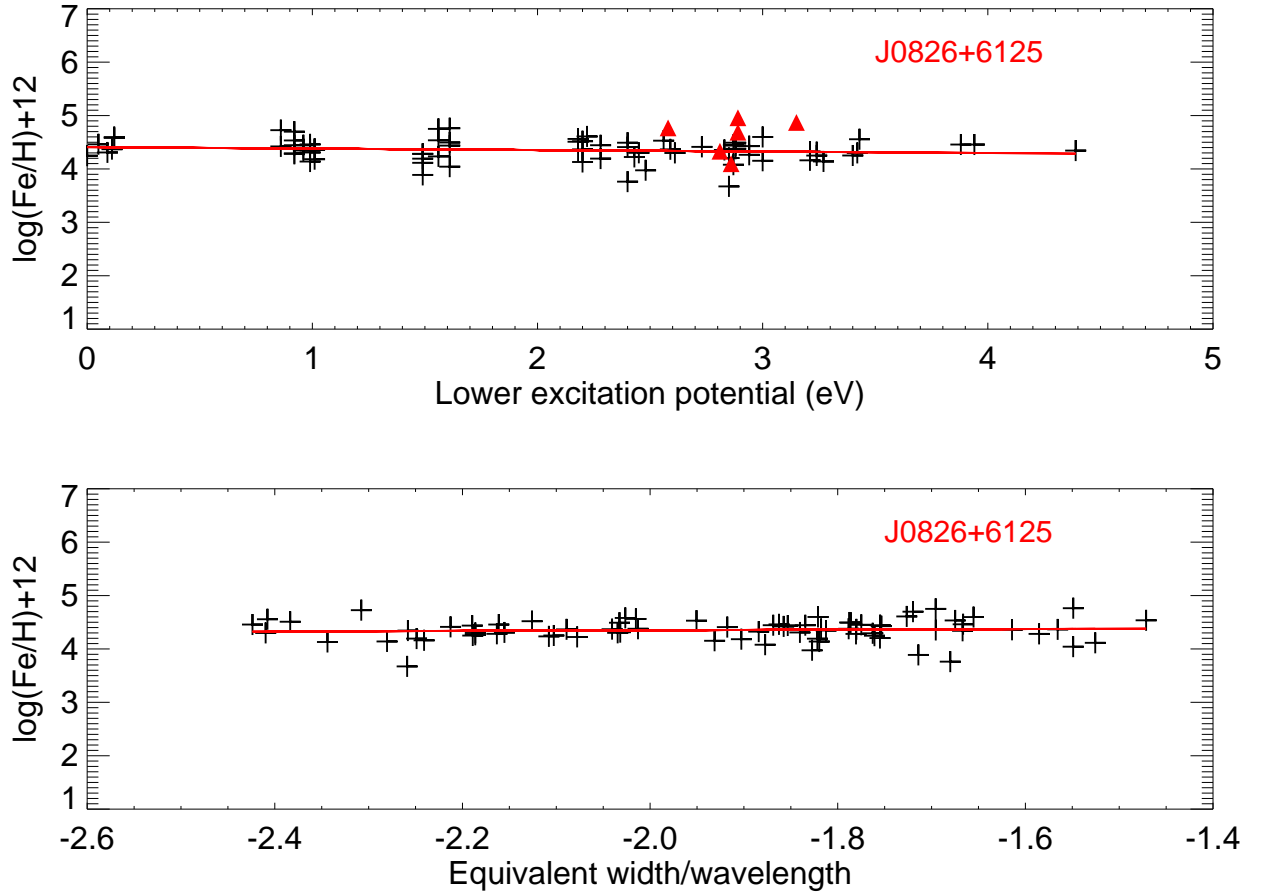


**Figure 5.** Top panel: Fe abundances derived from all lines, as a function of the lower excitation potential, for the adopted model for SDSS J0826+6125. Lower panel: Fe abundances, as a function of reduced equivalent widths, for the measured lines.

these corrections improves the agreement between the values of aluminum abundances obtained from this line and the high-excitation infrared doublet at 8773 Å, in the case of globular cluster dwarfs. Hence, we have applied this non-LTE correction to Al in our abundance table. Aluminum is slightly enhanced for SDSS J0826+6125, while Na tracks the iron content of the stars. The scandium content is also very similar to iron. Na and Al are produced by the Ne-Na and Mg-Al cycles in intermediate and massive stars during H-shell burning. Sodium and aluminum in the two stars could be due to a well-mixed ISM, and unlikely to have received direct contribution from intermediate-mass or massive-star winds.

#### 5.4. The Iron-Peak Elements

Iron abundances for SDSS J0826+6125 were calculated using 82 Fe I lines and 7 Fe II lines found in the spectra; a difference of 0.3 dex was noted between the derived abundances. This difference between Fe I and Fe II is in agreement with the NLTE effects explored by Asplund (2005). Iron abundances for SDSS J1341+4741 were calculated using 49 Fe I lines and 7 Fe II lines found in the spectra; a difference of 0.5 dex between the abundance values obtained from these lines was found, which is rather large.

We also detected the iron-peak elements Mn, Cr, Co, Ni, and Zn in our target stars. Mn and Cr are products of incomplete explosive silicon burning, and their abundances decrease with decreasing metallicity (McWilliam et al. 1995; Ryan et al. 1996; Carretta et al. 2002). For SDSS J0826+6125, the abundance of Mn was derived from the resonance Mn triplet at 4030 Å and three weaker lines near 4780 Å. Cr lines are measured from 4 lines, including the stronger ones at 4646 Å and 5206 Å. Products of complete silicon burning, such as Co, Ni, and Zn, have also been found in this star; all of these elements are found to track the iron content. For SDSS J1341+4741, the abundance of Mn was derived from the resonance Mn triplet at 4030 Å and an additional line at 3823 Å. The observed abundances of Mn and Cr are similar to other EMP stars. The abundance derived for Ni using the 4 lines of this element present in the spectrum of SDSS J1341+4741 is clearly higher relative to iron,  $[\text{Ni}/\text{Fe}] = +0.35$ .

#### 5.5. The Neutron-Capture Elements

Strontium and barium are the two neutron-capture elements detected in the spectra of SDSS J1341+4741. Resonance lines of Sr II at 4077 Å and 4215 Å are detected in both of our target stars. SDSS J0826+6125 is found to be under-abundant in both strontium and barium, with abundances of  $[\text{Sr}/\text{Fe}] = -0.63$  and  $[\text{Ba}/\text{Fe}] = -0.95$ , respectively. The other neutron-capture elements found in this star are Y and Zr, which are under-abundant as well. SDSS J1341+4741 is also found to be under-abundant in strontium compared to the solar ratio,  $[\text{Sr}/\text{Fe}] = -0.51$ . Ba II resonance lines at 4554 Å and 4937 Å were also measured, and exhibited a considerable barium depletion,  $[\text{Ba}/\text{Fe}] = -0.73$ . Based on the clear under-abundance of the neutron-capture elements, along with its strong carbon over-abundance, this star can be confidently classified as a CEMP-no star.

Best-fit spectra of the Sr and Ba syntheses for our two stars are shown in Figures 9 and 10.

#### 5.6. Lithium

Although lithium was not detected in SDSS J0826+6125, there is a strong feature observed in SDSS J1341+4741 at 6707 Å, the Li doublet, from which we obtain an abundance  $A(\text{Li}) = 1.95$ , which is similar to some other CEMP-no stars (e.g., Sivarani et al. 2006; Matsuno et al. 2017). The detection of lithium indicates that this star is unlikely to have experienced AGB binary mass transfer or direct winds from a massive star. Mass transfer from a low-mass AGB would produce large amounts of carbon and deplete lithium, along with the production of *s*-process enhanced material. A  $(4 - 7M_{\odot})$  AGB star that had experienced hot bottom burning produces large nitrogen and very low carbon. There are some models in which AGB stars could produce lithium through the Cameron-Fowler mechanism (Cameron & Fowler 1971). It is unclear if an AGB with mass  $3-4M_{\odot}$  could explain the observed C, N, low *s*-process elements, and lithium. Evolutionary mixing inside the star in its subgiant phase might deplete the original lithium abundance of the star-forming cloud. The synthesis for this element is shown in Figure 11.

### 6. DISCUSSION

#### 6.1. SDSS J082625.70+612515.10

##### 6.1.1. Carbon, Nitrogen, and the Non-detection of Lithium

In the *First Stars VI* paper, Spite et al. (2005) found that carbon and nitrogen were anti-correlated, and the faint halo stars could be classified into two groups – “unmixed” stars, which exhibited C enhancement with N depletion, having  $A(\text{Li})$  between 0.2 and 1.2, and “mixed” stars, which showed  $[\text{C}/\text{Fe}] < 0.0$ ,  $[\text{N}/\text{Fe}] > +0.5$ , and Li below the detection threshold. SDSS J0826+6125 clearly falls into the second group. Lithium is a very fragile element, which is destroyed at temperatures in excess of 2.5 million K. Evidence for this can be seen in previous samples of metal-poor stars; the  $A(\text{Li}) = 2.3$  observed for metal-poor dwarfs starts decreasing as the star ascends the giant branch, to  $A(\text{Li}) < 1.2$  for giants (*First Stars VII*; Bonifacio et al. 2007). The non-detection of lithium for this star could be understood in this way.

In *First Stars IX*, Spite et al. (2006) argued that such destruction could be taken as a signature of mixing, and placed this mixed group of stars higher up in the giant-branch stage of evolution. Other scenarios for depletion of lithium, such as binary mass transfer, can be eliminated for SDSS J0826+6125, as no such peculiar chemical imprints have been found. During mixing, material from deeper layers where carbon is converted to nitrogen is brought to the stellar surface. Figure 4 of Cayrel et al. (2004) shows the decline in the value of  $[\text{C}/\text{Fe}]$  for temperatures below 4800 K in metal-poor stars, which is again attributed to deep mixing at lower temperatures. With a  $T_{\text{eff}}$  of 4300 K and a low  $\log(g) = 0.4$ , SDSS J0826+6125 can be placed in the mixed group of stars close to the tip of the red giant branch (RGB). Figure 12 shows the position of the star in the  $\log(g)$ - $T_{\text{eff}}$  plane, compared with other metal-poor halo stars compiled in the SAGA database (Suda et al. 2008). It sits right at the tip of the RGB. Figure 13 compares the  $[\text{C}/\text{N}]$  ratio with metallicity of the halo stars having carbon deficiency (and for which both estimates of carbon and nitrogen are available). The abundance ratio of  $[\text{C}/\text{N}]$  for SDSS J0826+6125 is remarkably low compared to other stars at the tip of the RGB.

##### 6.1.2. The Light Elements

SDSS J0826+6125 exhibits a low Na, high Mg, and low Al content, consistent with the odd-even pattern expected to oc-

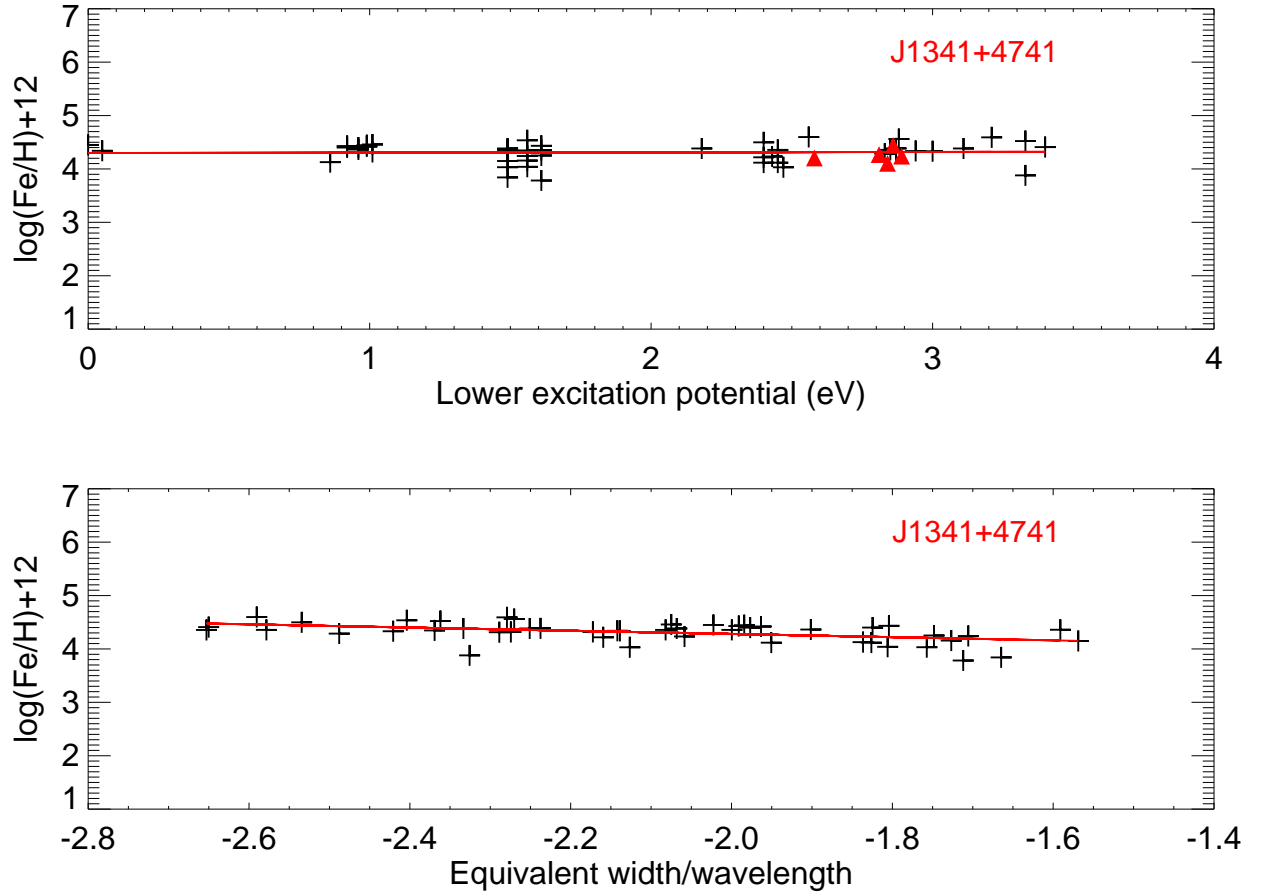


**Figure 6.** Top panel: Fe abundances derived from all lines, as a function of the lower excitation potential, for the adopted model for SDSS J1341+4741. Lower panel: Fe abundances, as a function of reduced equivalent widths, for the measured lines.

cur during massive-star nucleosynthesis at low metallicities. A slight enhancement of Na is observed, which could be an imprint of the previous generations of stars which underwent the Ne-Na cycle, as it is not possible to produce these elements in the RGB phase. Such an anomaly could be similar to that seen in globular cluster stars (Gratton et al. 2001, 2004), which have undergone the AGB phase and passed on processed material to a subsequent generation of star formation in a closed system. Unfortunately, other signatures seen in globular cluster stars, such as the C-N-O and O-Na-Mg-Al correlations and anti-correlations (Shetrone 1996; Gratton et al. 2004; Carretta et al. 2010; Coelho et al. 2011; Mészáros et al. 2015) were not observed in this star.

#### 6.1.3. The Iron-Peak Elements

Abundances of Fe-peak elements (Cr, Mn, Co, and Ni) for metal-poor stars from the SAGA database are plotted, as a function of metallicity, in Figure 14, along with the position of SDSS J0826+6125. This star appears to be relatively rich in Co, but poor in Cr, Mn, and Ni, consistent with McWilliam et al. (1995) and Audouze & Silk (1995), who showed the same trends for several stars with metallicity below  $[\text{Fe}/\text{H}] = -2.4$ . The relative abundances of the Fe-peak nuclei could be well-explained by their dependence on the mass cut of the progenitor supernova with temperature, which gives rise to a photo-disintegration process (Woosley & Weaver 1986).

#### 6.1.4. The Neutron-Capture Elements

Abundances of both the heavy and light *s*-process elements found in SDSS J0826+6125 are low, which is again consistent with the lack of available neutron flux (Audouze & Silk 1995). The abundance values are very similar to other EMP giants.

#### 6.1.5. The Asymmetric $H\alpha$ Profile of SDSS J0826+6125

SDSS J0826+6125 was observed several times, and an asymmetry in the  $H\alpha$  profile was noted for all of the spectra. The profile also could not be well-fit with synthetic spectra. The  $H\alpha$  profile and its fit with the model spectrum is shown in Figure 15. This could be due to the inadequacy of the 1D stellar models, or it may be due to an extended atmosphere present in the star. The  $H\alpha$  profile was also found to be not varying over several observation epochs indicating no ongoing mass transfer. The extended atmosphere could be the result of past mass transfer from an intermediate-mass AGB companion, or mixing due to first dredge up of the star in the RGB phase. It is also possible that the star itself is an AGB star (e.g., Masseron et al. 2006).

### 6.2. SDSS J134144.60+474128.90

#### 6.2.1. Lithium

We have obtained a measurement of  $A(\text{Li}) = 1.95$  for SDSS J1341+4741, which is lower than the Spite Plateau (Spite & Spite 1982) value of  $A(\text{Li}) = 2.2 \pm 0.1$  (Pinsonneault et al. 1999), and much lower than the predicted amount of Li from Big Bang nucleosynthesis ( $A(\text{Li}) = 2.75$ ; Steigman 2005). Our limited RV information for this star indicates clear variation, from which we derive a possible period of 116 days. However, we have no other evidence that a mass-transfer event may have occurred. The distribution of lithium for CEMP-no stars, along with other EMP stars, is shown in Figure 16. According to the analysis of Meynet et al. (2010) and Masseron et al. (2012), this star falls close to the edge

of Li-depleted stars ( $A(\text{Li}) = 2.00$  is adopted as the separation between Li-normal and Li-depleted metal-poor stars). A slight depletion from the Spite Plateau value could be attributed to internal mixing of the star, or the observed value of lithium for SDSS J1341+4741 may be the result of several concurrent phenomena.

- The ejected material from the progenitor SN will have depleted lithium abundance along with other nucleosynthetic elements and enhanced carbon (for the case of SDSS J1341+4741) that is mixed with the primordial cloud. Depending upon the dilution factor in the natal cloud, it may be possible to achieve the necessary lithium value (Piau et al. 2006; Meynet et al. 2010; Maeder et al. 2015).
- A Spite Plateau value of Li was present in the natal cloud of SDSS J1341+4741, and it is depleted by thermohaline mixing or meridional circulation (Masseron et al. 2012) in the star. If we consider the current evolutionary state of the star to be in the RGB phase, this could be a viable mechanism.
- Enhanced rotationally-induced mixing in the RGB phase (following Denissenkov & Herwig 2004) can lead to formation of lithium in the star, following depletion of all the primordial lithium. It is very difficult to differentiate between an AGB or a massive rotating star as the precursor using Li as the sole yardstick, as both result in almost the same nucleosynthetic yield of Li (Meynet et al. 2006; Masseron et al. 2012).

#### 6.2.2. Carbon

According to Spite et al. (2013) and Bonifacio et al. (2015), CEMP stars are distributed along two bands in the  $A(\text{C})$  vs.  $[\text{Fe}/\text{H}]$  plane. The upper band is centered around  $A(\text{C}) \sim 8.25$ , and comprises relatively more metal-rich CEMP-*s* stars, while the lower band centered around  $A(\text{C}) \sim 6.50$  comprises more metal-poor, and primarily CEMP-no, stars. Further investigation by Hansen et al. (2016a) also led the result that the majority of the stars that are known binaries lie close to the upper band.

By expanding the list of CEMP stars with available high-resolution spectroscopic analyses to include more evolved sub-giants and giants (with the later giants having C abundances corrected for evolutionary mixing effects; Placco et al. 2014), Yoon et al. (2016) demonstrated that the morphology of this abundance space is more complex, with three prominent groups identified in the so-called Yoon-Beers diagram (their Figure 1). They argued that a separation between CEMP-*s* stars and CEMP-no stars in their sample could be reasonably achieved by splitting the sample at  $A(\text{C}) = 7.1$ , with the Group I CEMP-*s* stars lying above this level and the Group II and III CEMP-no stars lying below this level. In this classification scheme, SDSS J1341+4741, with  $A(\text{C}) \sim 6.22$ , can be comfortably identified as a Group II CEMP-no star. Hence, the enhancement of carbon in this star is most likely to be intrinsic to the star (i.e., the C was present in its natal gas), and not the result of mass transfer from an extinct AGB companion. Thus, the elemental-abundance pattern observed from this star is associated with nucleosynthesis from a core collapse SN at early times, perhaps with additional contributions from stars that formed and evolved within its natal gas cloud.

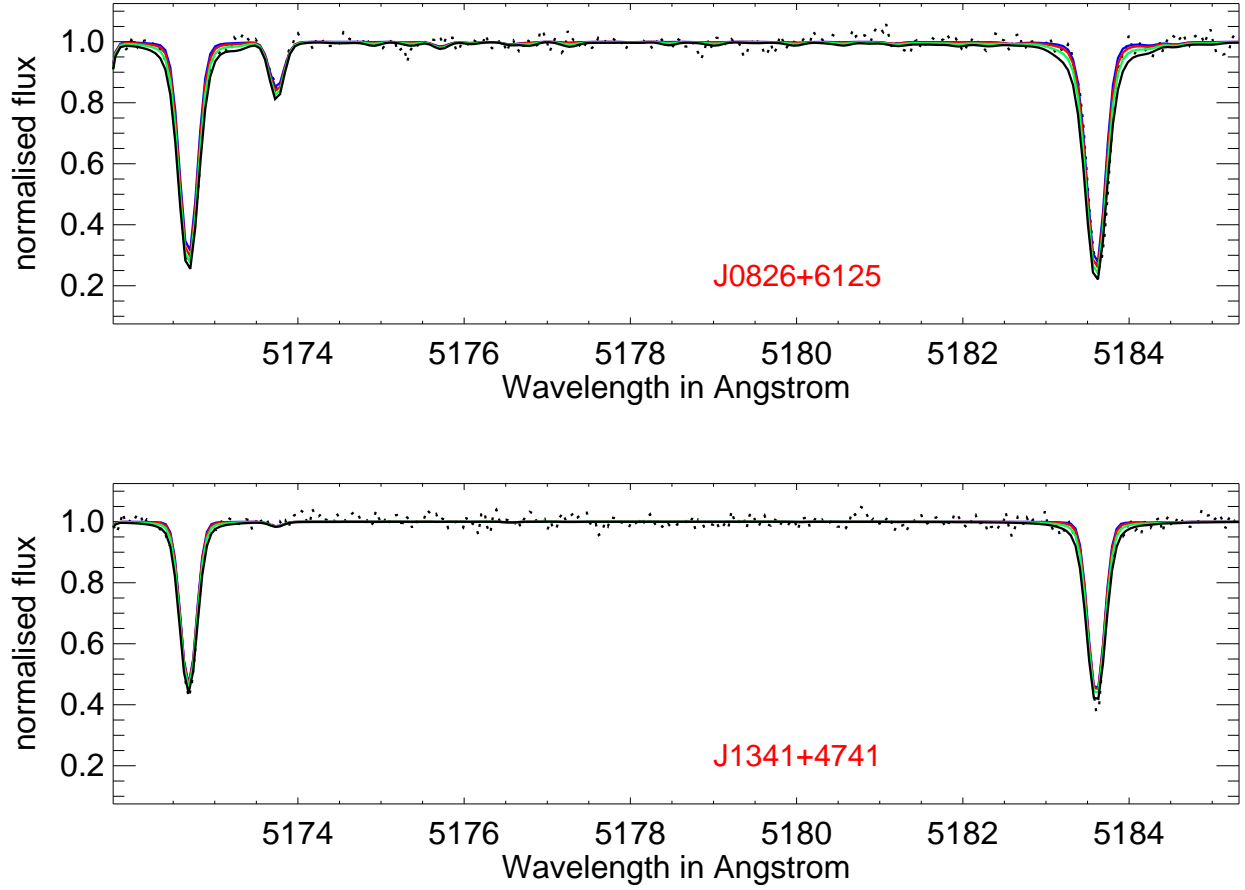


**Figure 7.** High-resolution HESP spectra of SDSS J0826+6125 (upper panel) and SDSS J1341+4741 (lower panel) in the region of the Mg I triplet for different values of  $\log(g)$ , in steps of 0.25 dex. The red solid line indicates the best-fit synthetic spectrum. The adopted parameters for SDSS J0826+6125 are  $T_{\text{eff}} = 4300$  K and  $\log(g) = 0.40$ , while those for SDSS J1341+4741 are  $T_{\text{eff}} = 5450$  K and  $\log(g) = 2.50$ .

### 6.2.3. The Light Elements

SDSS J1341+4741 exhibits the low  $[\text{Na}/\text{Fe}]$ , high  $[\text{Mg}/\text{Fe}]$ , and low  $[\text{Al}/\text{Fe}]$  ratios expected from the odd-even pattern in massive-star nucleosynthesis yields at low metallicities (e.g., Arnett 1971; Truran & Arnett 1971; Peterson 1976; Umeda et al. 2000; Heger & Woosley 2002). The light elements closely follow the overall halo population observed in the Galaxy as well (Cayrel et al. 2004). Following Yoon et al. (2016), SDSS J1341+4741 is clearly a member of the Group II stars, and supports a possible mixing and fallback SN as a likely progenitor.

### 6.2.4. The Iron-Peak Elements

Abundances of Fe-peak elements for SDSS J1341+4741 (Cr, Mn, Co, and Ni) are shown in Figure 14, as a function of  $[\text{Fe}/\text{H}]$ , compared with other CEMP-no and C-normal EMP stars compiled from the SAGA database (Suda et al. 2008). One feature that clearly stands out is the over-abundance of Cr and Ni, and to some extent Mn. In the low-metallicity regime, the stars are expected to show signatures of Type II SNe nucleosynthesis. All three elements play key roles in determining the progenitor population in the halo and the subsequent SNe yields. A decrease in  $[\text{Cr}/\text{Fe}]$  and  $[\text{Mn}/\text{Fe}]$  with decreasing  $[\text{Fe}/\text{H}]$  should be accompanied with enhancement in  $[\text{Co}/\text{Fe}]$ , as a result of deeper mass cuts in the progenitor SNe (refer to Figure 9 of Nakamura et al. 1999). However, enhancement in both  $[\text{Cr}/\text{Fe}]$  and  $[\text{Mn}/\text{Fe}]$  can be explained by an excess of neutrons as well. Since neutron excess is a function of metallicity, we have plotted  $[\text{Cr}/\text{Fe}]$  vs.  $[\text{Mn}/\text{Fe}]$  in Figure 17 to eliminate the trend with Fe abundance (following, e.g., Carretta et al. 2002). In this plot, our program star occupies a relatively higher position amidst the population of CEMP-no stars. From Heger & Woosley (2002), Heger & Woosley (2010), and Qian & Wasserburg (2002), it is known that very massive stars ( $80 < M/M_{\odot} < 240$ ) belonging to Population III explode as pair-instability SNe, which should not produce a correlation between  $[\text{Cr}/\text{Fe}]$  and  $[\text{Mn}/\text{Fe}]$ . Thus, the presence of this correlation points us towards Type II SNe associated with a relatively high-mass ( $M/M_{\odot} < 80$ ), but not extremely high-mass, progenitor.

Nickel is an extremely important element to gain further insight into the nature of the progenitor of SDSS J1341+4741. The depth of the gravitational potential and amount of neutrino-absorbing material in the models are the two factors that compete for the production of Ni in Type II SNe. In very massive ( $M/M_{\odot} > 30$ ) stars the deeper gravitational potential restricts nickel from being ejected due to fallback, while intermediate-mass ( $10 < M/M_{\odot} < 20$ ) stars eject large amounts of Ni because of a large neutrino-absorbing region (Nakamura et al. 1999). Thus, enhancement of Ni also points in the same direction, that the progenitor is likely to be a massive ( $20 < M/M_{\odot} < 30$ ) star exploding as a Type II SNe in the early Galaxy. The observations support the hypothesis of a mixing and fallback model (Nomoto et al. 2013) with a lower degree of fallback, so as to eject a larger mass of  $^{56}\text{Ni}$ .

### 6.2.5. The Neutron-Capture Elements

The first *s*-process peak element Sr and the second *s*-process peak element Ba have been detected in both SDSS J0826+6125 and SDSS J1341+4741, and they exhibit under-abundances. The ratio of light to heavier neutron-capture elements are sensitive to the nature of the progen-

itors. Neutron star mergers are expected to produce heavy neutron-capture elements (e.g., Argast et al. 2004) – and have been observed to do so in the kilonova SSS17a associated with GW170817 (Kilpatrick et al. 2017), which exhibited clear evidence for the presence of unstable isotopes created by the *r*-process (Droett et al. 2017; Shappee et al. 2017). SNe with jets (e.g., Winteler et al. 2012; Nishimura et al. 2015) may also produce heavy neutron-capture elements. Formation of these systems may depend on the environment as well.

### 6.2.6. Nature of the Binary Companions of SDSS J0826+6125 and SDSS J1341+4741

Both of the program stars exhibit clear RV variations, indicating the likely presence of a binary companion. In the case of SDSS J0826+6125, the enhanced abundances of N and under-abundance of C indicates possible mixing of the atmosphere with CN-cycle products. This can result from first dredge-up mixing in the star, which is currently in the RGB, following mass transfer from an intermediate-mass AGB star that might have gone through hot bottom burning (Lau et al. 2007; Suda et al. 2012). The low  $\log(g)$  value of the star supports RGB mixing, although AGB mass transfer cannot be ruled out. The non-detection of Li and peculiar  $\text{H}\alpha$  profiles could indicate either internal mixing or binary mass transfer as well. In the case of an intermediate-mass AGB that goes through hot bottom burning, the temperatures are sufficiently high for the star to operate the CNO cycle. In that case, SDSS J0826+6125 may be a true nitrogen-enhanced metal-poor (NEMP; see Johnson et al. 2007; Pols et al. 2009; Pols et al. 2012) star, which are known to exist, but are relatively rare.

In the case of SDSS J1341+4741, the binary companion did not likely contribute through a mass-transfer event, since the Li abundance in the star is similar to other EMP stars, although it is lower than the Spite Plateau value. The mild depletion of Li could be due to binary-induced mixing or internal mixing of the star during its sub-giant phase. It may well be worthwhile to mount a RV-monitoring campaign for this and other Li-depleted EMP stars to test for a possible binary-star origin to the declining lithium abundance problem for stars with  $[\text{Fe}/\text{H}] < -3.0$ .

### 6.3. CEMP-no and EMP Stars

From the above discussion, and based on previous studies, it is evident that CEMP-no and C-normal EMP stars have very different origins. Even within the sub-class of CEMP-no stars, there may well be different types of progenitors. As discussed by Yoon et al. (2016), the Group II CEMP-no stars could be associated with the faint mixing and fallback SNe, whereas the Group III CEMP-no stars can be attributed to the spinstar models, with a number of exceptions for both the classes (Meynet et al. 2006; Nomoto et al. 2013). See also the discussion of the progenitors for CEMP-no stars by Placco et al. (2016). Some of the CEMP-no stars lying in the low  $A(\text{C})$  region may have a binary component, but no mass transfer is supposed to have taken place (Starkenburg et al. 2014; Bonifacio et al. 2015; Yoon et al. 2016), which is further strengthened by the only “slight” depletion of Li in SDSS J1341+4741, as described in the previous section. Iron-peak elements can provide valuable insights regarding the nucleosynthetic yields of their progenitor supernovae, as these elements cannot be produced or modified during the post main-sequence evolutionary stages of the star. Figure 14 shows the distribution of some key Fe-peak elements for both

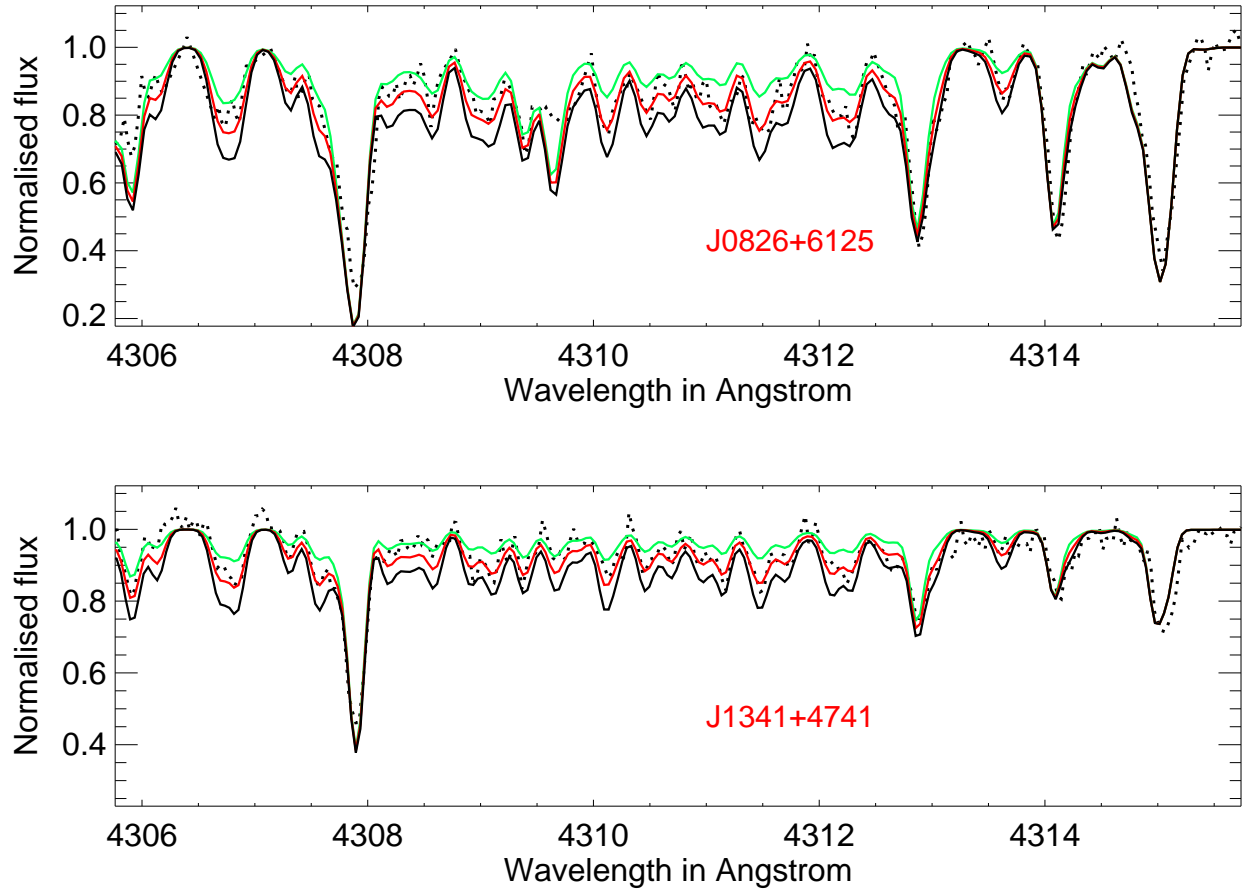


**Figure 8.** High-resolution HESP spectra in the CH  $G$ -band region for SDSS J0826+6125 (upper panel) and SDSS J1341+4741 (lower panel). The red solid line indicates the synthetic spectrum corresponding to the best fit, overplotted with two synthetic spectra with carbon 0.20 dex higher and lower than the adopted value.

CEMP-no and C-normal EMP stars. Visual inspection suggests that Cr and Co are enhanced for the CEMP-no population. We have compiled data from SAGA database to see if there is an enhancement of Cr in CEMP-no stars. The fit is given in Figure 18 for  $[\text{Cr}/\text{Fe}]$ . There is a slight offset between the EMP and CEMP-no stars, but they exhibit similar increasing trends of  $[\text{Cr}/\text{Fe}]$  with  $[\text{Fe}/\text{H}]$ . We have checked, and these behaviors apply to both dwarfs and giants. Similar offset could also be noted for Co. Lai et al. (2008) and Bonifacio et al. (2009) have considered the discrepancies in the behavior of Cr between giants and dwarfs, since Cr II could be measured only in giants, while Cr I is a resonance line, and could suffer substantial NLTE effects. However, such issues are not expected to play a substantial role when we compare only giants with giants or dwarfs with dwarfs. Temperature and gravity do not play a major role in deviations from LTE abundances (Bergemann & Cescutti 2010), so we have not used them to further refine our sample from the archival data. Enhancement in  $[\text{Cr}/\text{Fe}]$  for CEMP-no stars with respect to C-normal EMP stars can play a key role for understanding of the SNe ejecta and relevant mass cuts. It would be very interesting to investigate the origin for this discrepancy.

## 7. CONCLUSION

We have derived LTE abundances for SDSS J082625.70+612515.10; it is mostly consistent with behavior of other halo stars. The depletion in carbon and enhancement in nitrogen could be due to internal mixing within the star. It is unlikely that self enrichment similar to that is seen in globular clusters has occurred, due to the overabundance in oxygen. The peculiar  $\text{H}\alpha$  profiles of SDSS J0826+6125 also supports the possibility of mixing that might occur in an extended atmosphere. The radial-velocity variation strongly suggests this star is a member of a binary system, but it is likely there is no ongoing mass transfer, due to non-variable peculiar  $\text{H}\alpha$  profile over a period of year.

SDSS J134144.60+474128.90 is a CEMP-no type star, and likely to be a member of binary system. The lithium is detected and mildly depleted, similar to other EMP stars. Lithium in EMP dwarfs and CEMP-no stars exhibit similar trends at different metallicities. Below  $[\text{Fe}/\text{H}] < -3.0$ , EMP and CEMP-no stars often have lithium abundance below the Spite Plateau. We also studied the trends of heavy elements among EMP and CEMP stars. At a given metallicity, CEMP-no stars appear to have larger abundances of Cr. This might provide important clues to the nature of the progenitors that contributed to the origin of carbon.

## 8. ACKNOWLEDGEMENT

We would like to take this opportunity to thank the HESP team for successful installation and maintenance of the high-resolution spectroscopy at the Hanle telescope, despite the numerous challenges and hurdles that were encountered along the way. We would specially like to thank Amit Kumar, M N Anand, Sriram and Kathiravan for their efforts. We also extend our gratitude towards the observation team, namely Kiran B.S, Pramod Kumar, Lakshmi Prasad and Venkatesh Shankar for their tireless effort.

T.C.B. acknowledges partial support from grant PHY 14-30152 (Physics Frontier Center/JINA-CEE), awarded by the U.S. National Science Foundation (NSF). T.M. acknowledges support provided by the Spanish Ministry of Economy and

Competitiveness (MINECO) under grants AYA201458082-P and AYA-2017-88254-P.

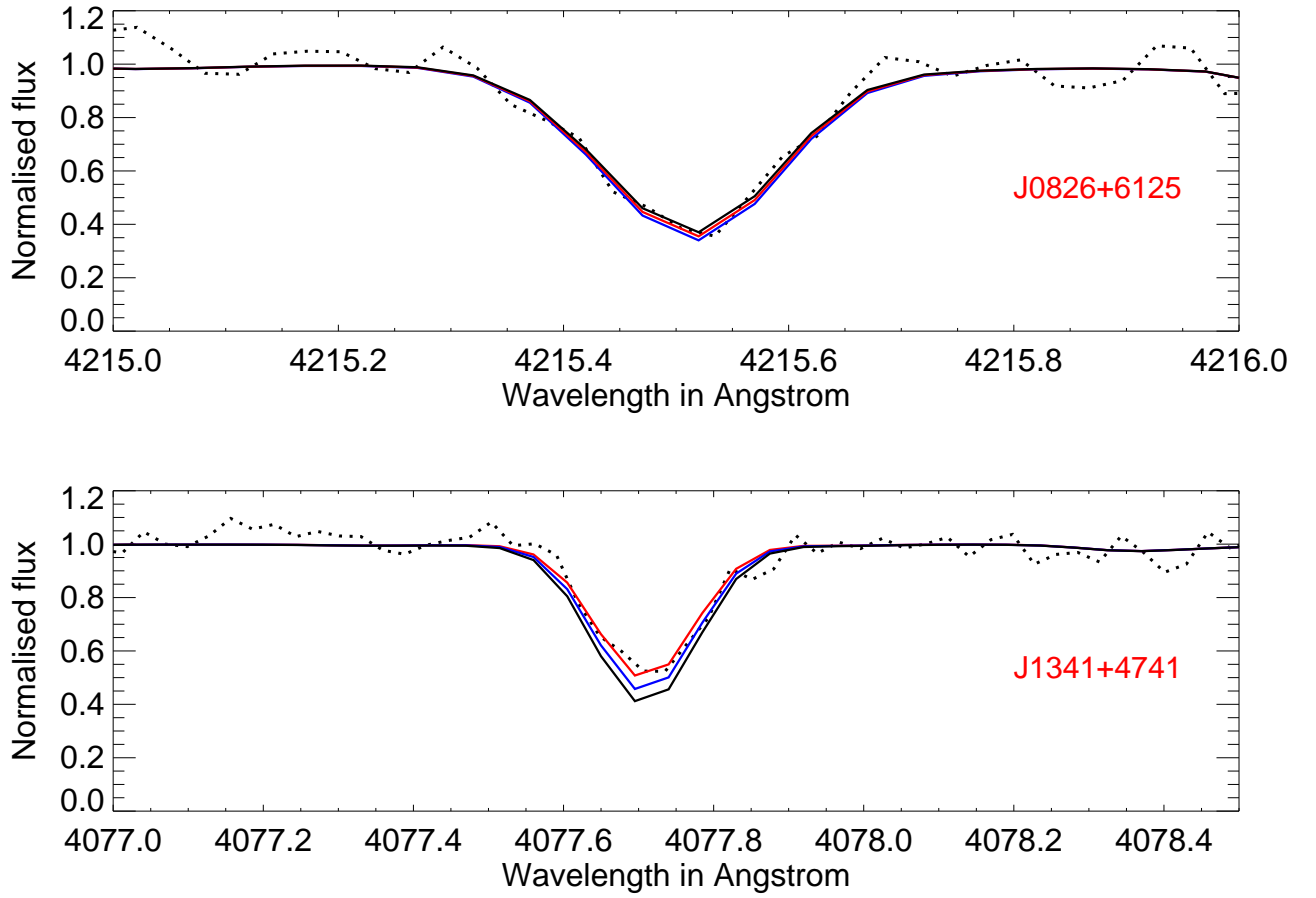


**Figure 9.** Synthesis in the Sr II region for SDSS J0826+6125 (upper panel) and SDSS J1341+4741 (lower panel). The red line indicates the best-fit, overplotted with two synthetic spectra with Sr abundance 0.20 dex higher and lower than the adopted value.

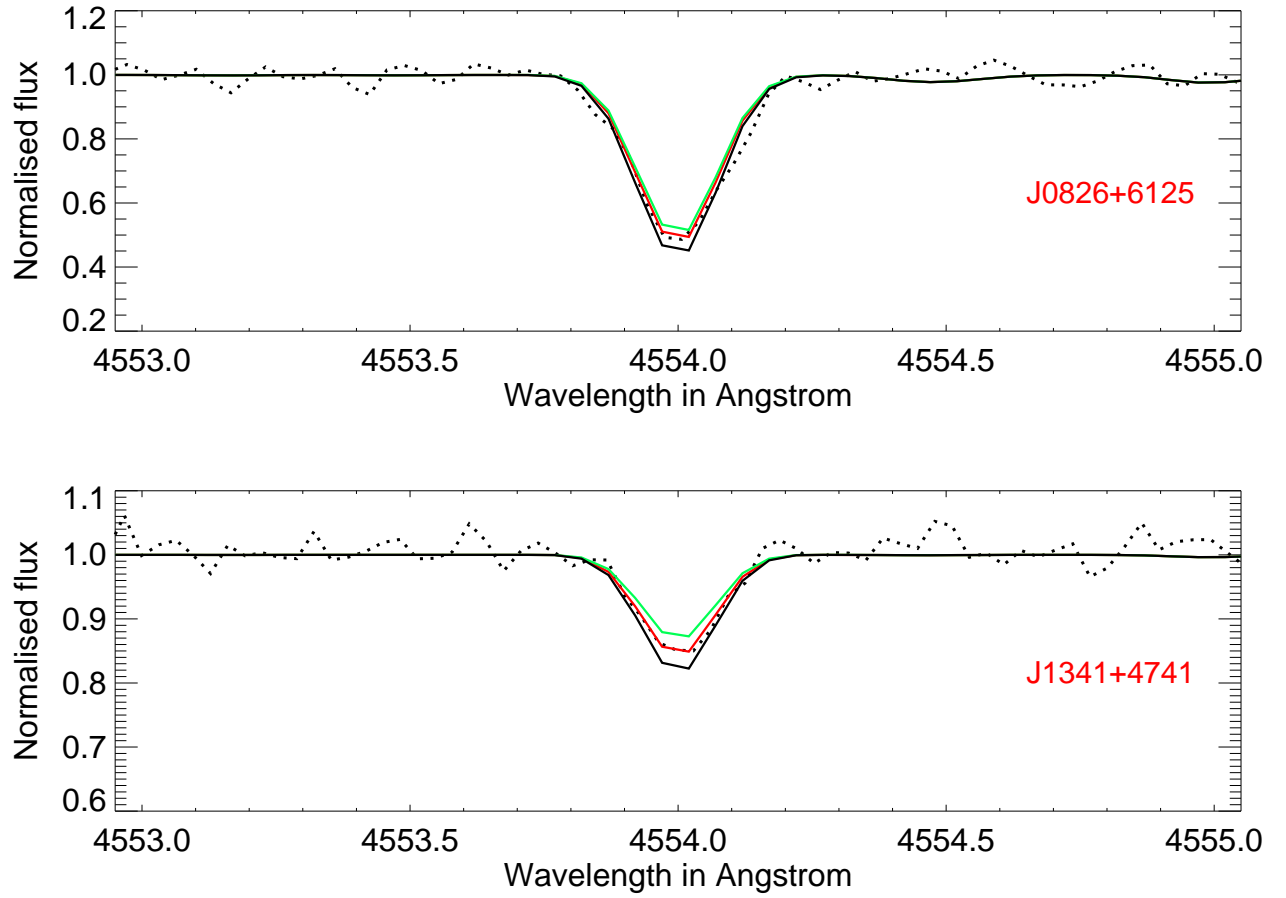


**Figure 10.** Synthesis in the Ba II region for SDSS J0826+6125 (upper panel) and SDSS J1341+4741 (lower panel). The red line indicates the best-fit, overplotted with two synthetic spectra with Ba abundance 0.20 dex higher and lower than the adopted value.

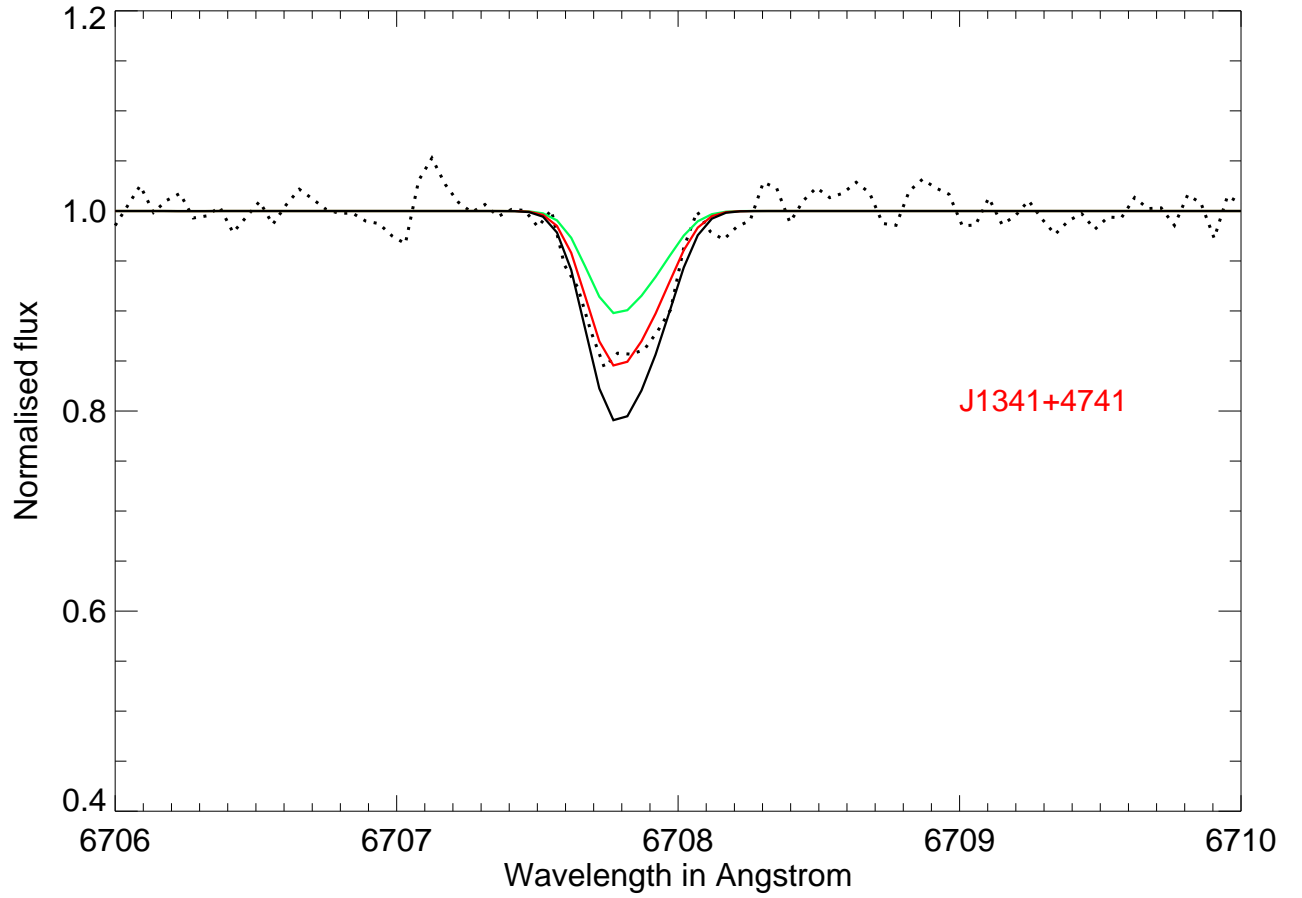


**Figure 11.** Synthesis of lithium for SDSS J1341+4741 at 6707 Å. The red line indicates the best-fit, overplotted with two synthetic spectra with Li abundance 0.20 dex higher and lower than the adopted value of  $A(\text{Li}) = 1.95$ .

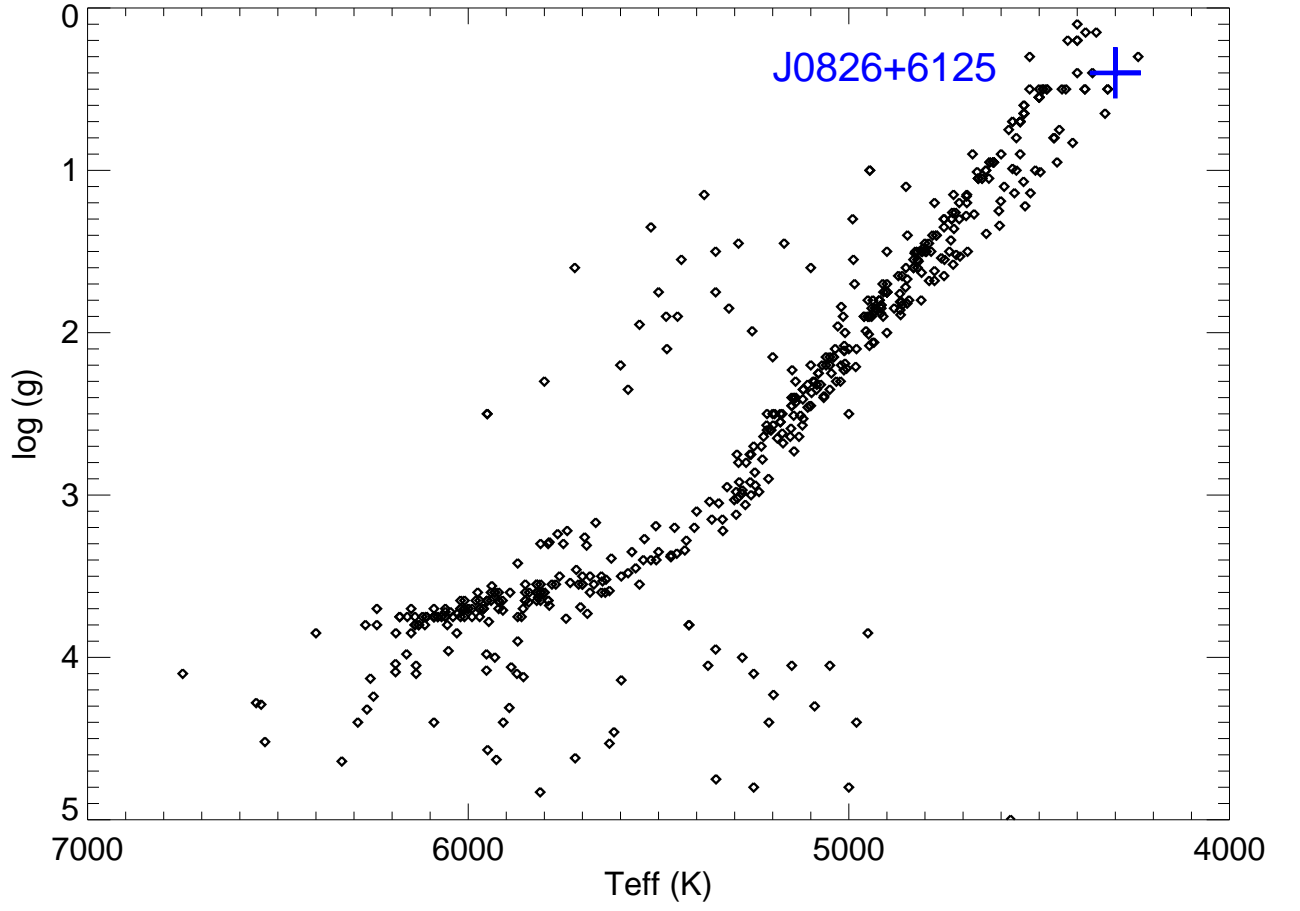


**Figure 12.** The position of SDSS J0826+6125 among other EMP halo stars in the  $\log(g)$ - $T_{\text{eff}}$  plane. The position of the star at the tip of the RGB is marked by the blue cross.

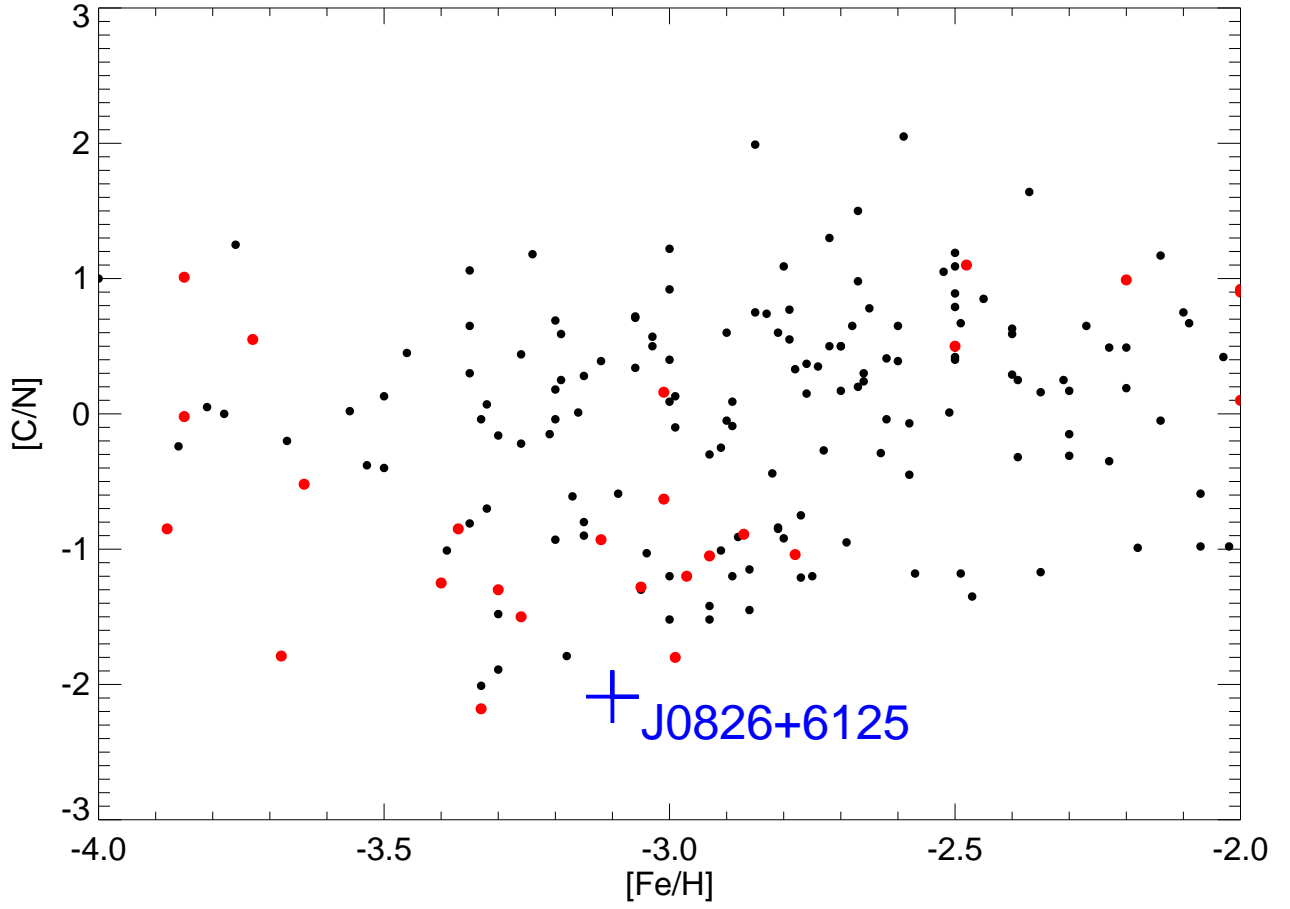


**Figure 13.** The very low  $[C/N]$  abundance ratio other low-metallicity C-poor halo stars. SDSS J0826+6125 is marked by the blue cross. The red dots mark the stars at the tip of the RGB with  $\log(g) < 1$ .

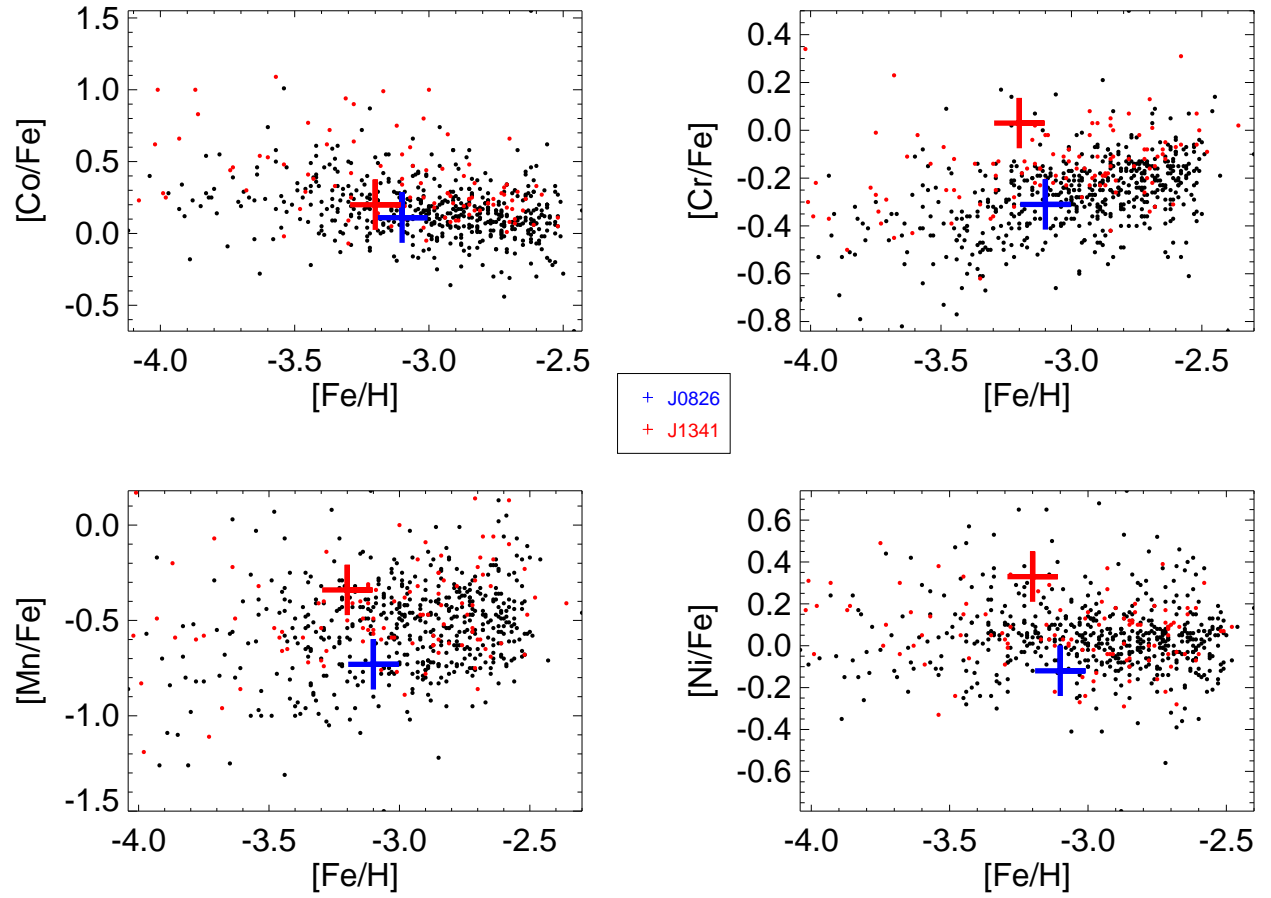


**Figure 14.** Distribution of Fe-peak elements for Galactic halo stars. The red dots represent the CEMP-no stars, while black dots represent C-normal halo stars. The two program stars SDSS J0826+6125 and SDSS J1341+4741 are indicated by blue and red crosses, respectively.

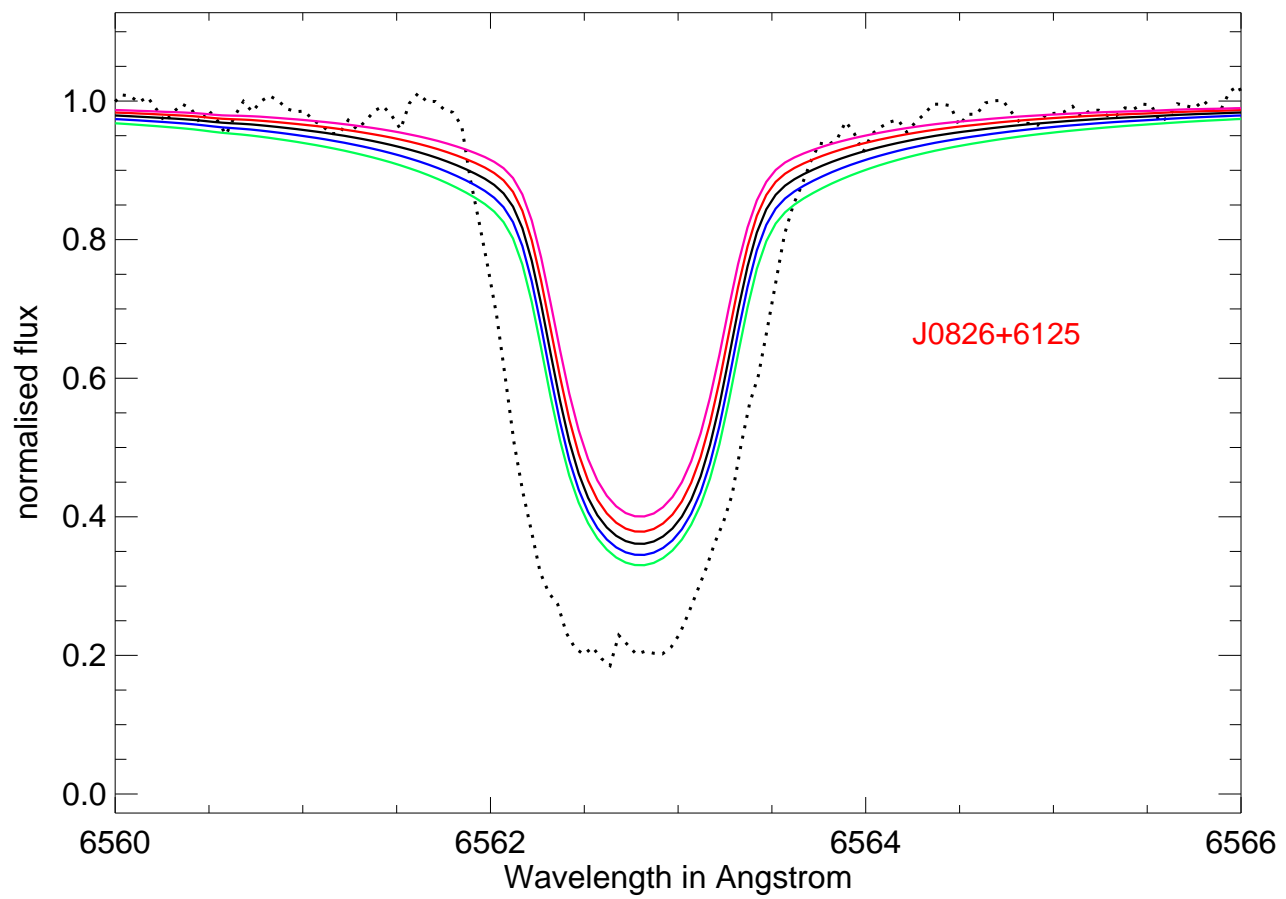


**Figure 15.** The strange H $\alpha$  profile of SDSS J0826+6125, for different values of temperature from 4200 K to 4600 K, in steps of 100 K.

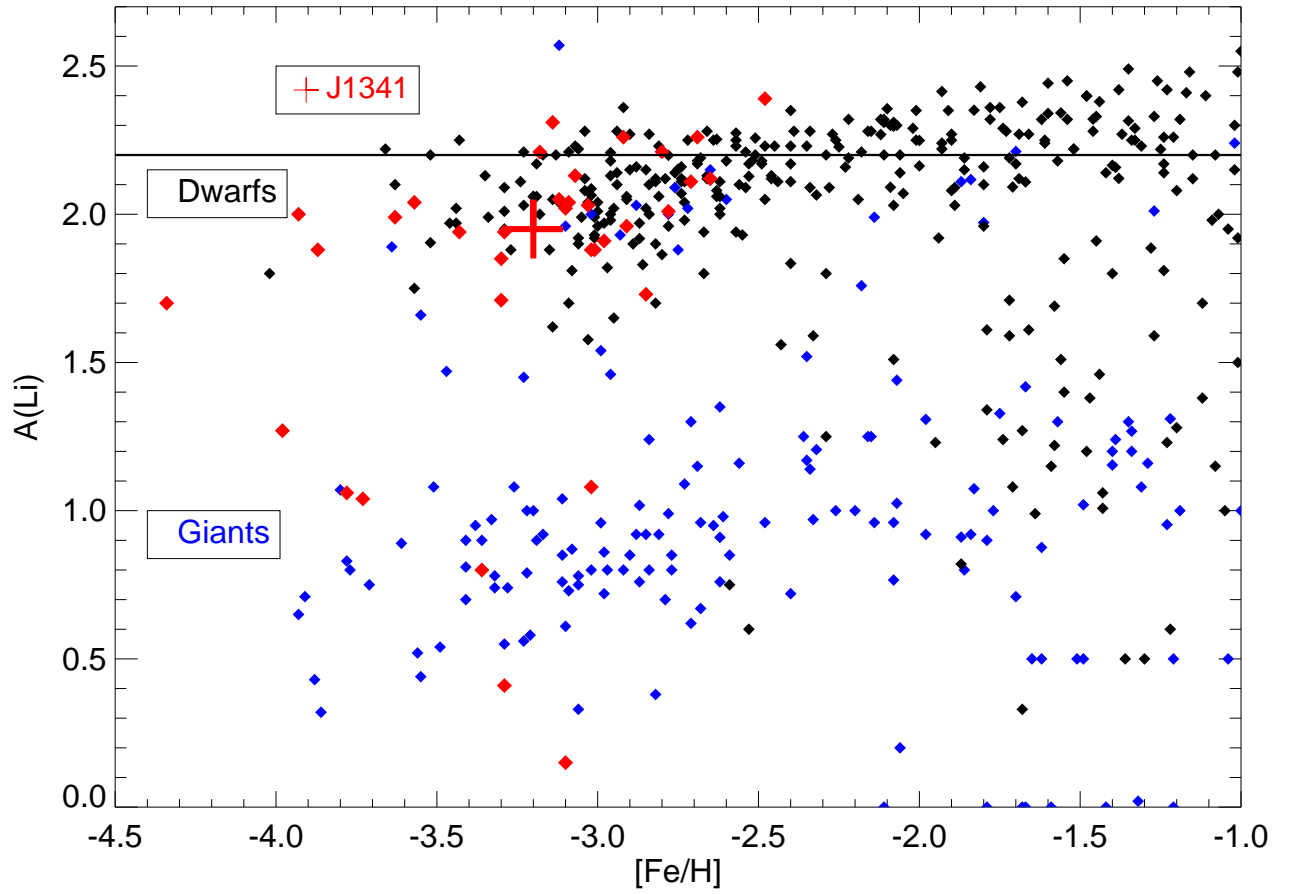


**Figure 16.** Comparison of the observed lithium for CEMP-no stars, taken from the SAGA Database. The blue dots mark the EMP giants while black dots are the EMP dwarfs. Red points are the CEMP-no stars. The red cross marks the location of SDSS J1341+4741.

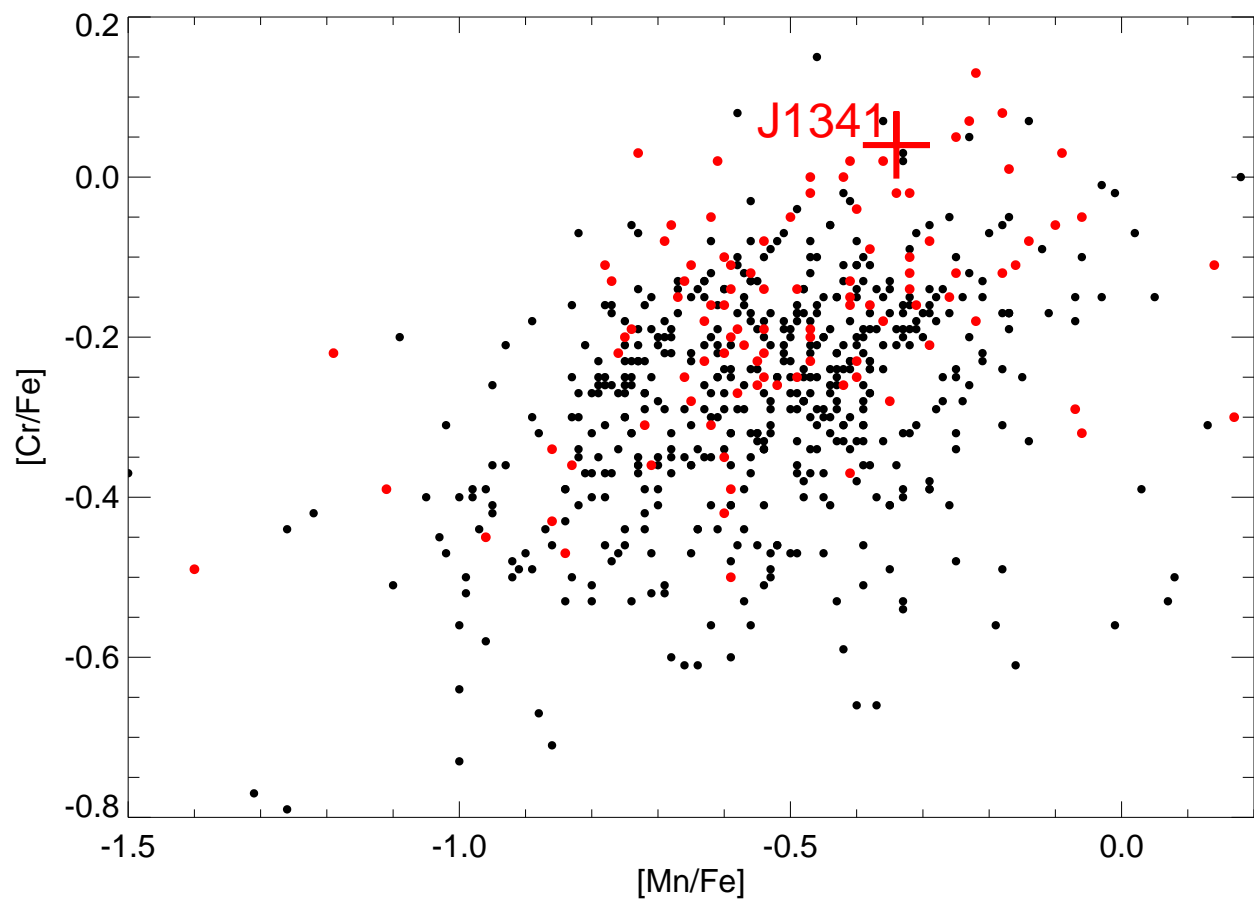


**Figure 17.** The relative enhancement of Cr and Mn for SDSS J1341+4741, shown as a red cross, in the  $[Cr/Fe]$  vs.  $[Mn/Fe]$  space. Red dots mark the CEMP-no stars while the black dots mark the EMP stars.

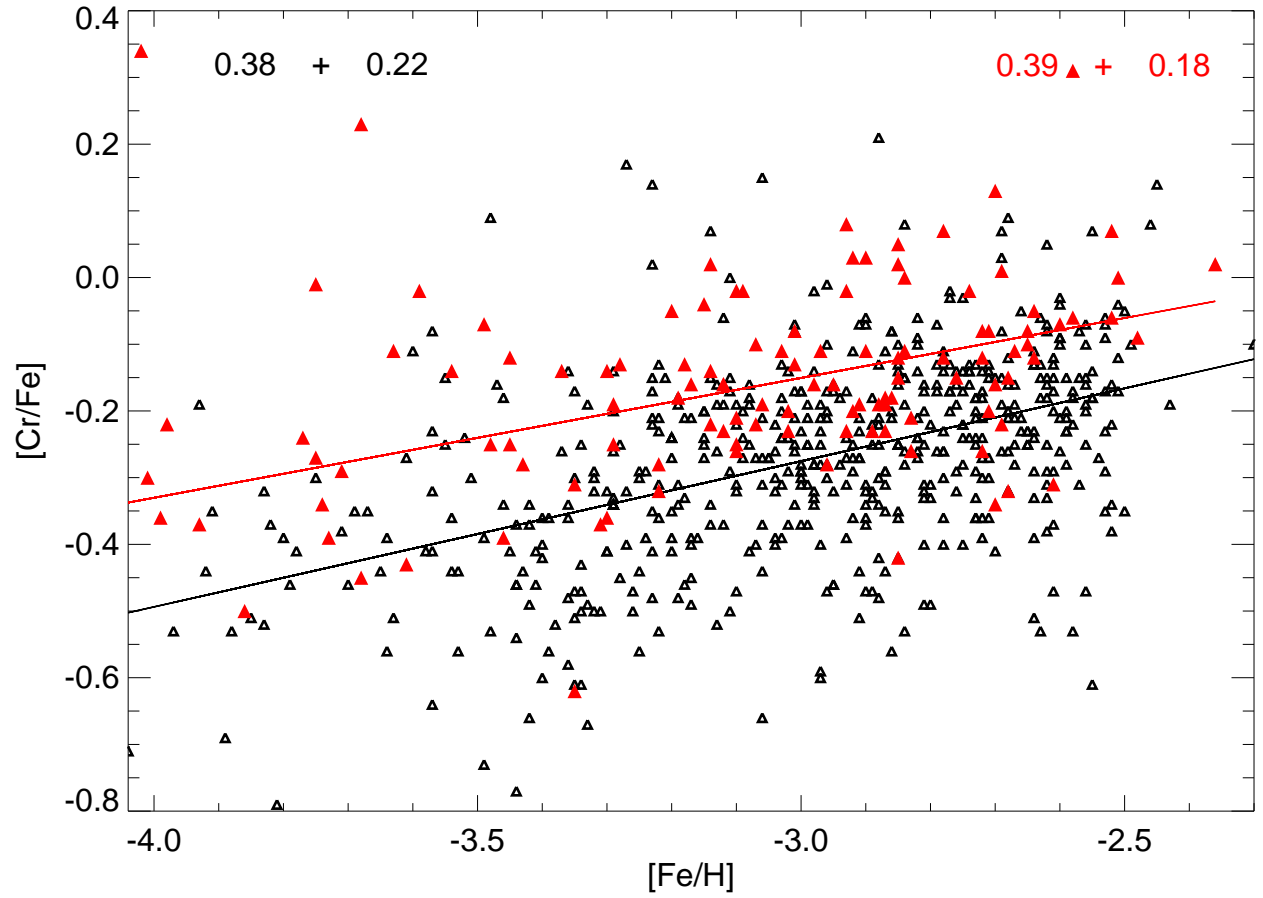


**Figure 18.** Linear fit for CEMP-no and C-normal EMP stars. Red is used for CEMP-no stars while black is used for EMP stars. The slope and  $\sigma$  are shown for each fit in the corresponding color.

## APPENDIX

**Table 7**  
Linelist for SDSS J0826+6125

| Species | $\lambda$ | obs.eqw | error <sup>*</sup> | Abundance |
|---------|-----------|---------|--------------------|-----------|
| CaI     | 4425.437  | 34.000  | 1.806              | 3.284     |
| CaI     | 4435.679  | 27.600  | 1.628              | 3.239     |
| CaI     | 5594.462  | 30.300  | 1.705              | 3.574     |
| CaI     | 6122.217  | 61.900  | 2.437              | 3.729     |
| CaI     | 6162.173  | 82.000  | 2.805              | 3.867     |
| CaI     | 6439.075  | 53.600  | 2.268              | 3.598     |
| CaI     | 6449.808  | 8.000   | 0.876              | 3.870     |
| TiI     | 4981.731  | 54.800  | 2.293              | 1.884     |
| TiI     | 4991.065  | 52.700  | 2.249              | 1.970     |
| TiI     | 4999.503  | 40.600  | 1.974              | 1.851     |
| TiI     | 5007.210  | 52.100  | 2.236              | 2.188     |
| TiI     | 5014.187  | 49.600  | 2.182              | 2.301     |
| TiI     | 5064.653  | 30.200  | 1.702              | 1.804     |
| TiI     | 5210.385  | 43.000  | 2.031              | 1.905     |
| TiII    | 4470.857  | 45.400  | 2.087              | 2.107     |
| TiII    | 5129.152  | 39.400  | 1.945              | 2.068     |
| TiII    | 5154.070  | 44.900  | 2.076              | 2.275     |
| TiII    | 5185.913  | 28.000  | 1.639              | 1.913     |
| TiII    | 5188.680  | 72.500  | 2.638              | 2.054     |
| TiII    | 5381.015  | 36.100  | 1.861              | 2.234     |
| CrI     | 4545.945  | 7.700   | 0.860              | 1.986     |
| CrI     | 4646.148  | 44.400  | 2.064              | 2.445     |
| CrI     | 5206.038  | 81.300  | 2.793              | 2.170     |
| CrI     | 5298.277  | 10.600  | 1.009              | 1.915     |
| CrI     | 5348.312  | 6.700   | 0.802              | 1.849     |
| CrII    | 4558.650  | 8.500   | 0.903              | 2.249     |
| CrII    | 4588.199  | 11.400  | 1.046              | 2.574     |

| Species | $\lambda$ | obs.eqw | error <sup>*</sup> | Abundance |
|---------|-----------|---------|--------------------|-----------|
| FeI     | 4147.669  | 68.747  | 2.569              | 4.283     |
| FeI     | 4174.913  | 72.100  | 2.631              | 4.513     |
| FeI     | 4175.636  | 23.000  | 1.486              | 3.837     |
| FeI     | 4202.029  | 125.300 | 3.468              | 4.195     |
| FeI     | 4206.697  | 90.700  | 2.950              | 4.492     |
| FeI     | 4216.220  | 119.900 | 3.392              | 10.028    |
| FeI     | 4233.603  | 63.000  | 2.459              | 3.989     |
| FeI     | 4250.787  | 143.600 | 3.712              | 4.707     |
| FeI     | 4260.474  | 89.000  | 2.923              | 3.780     |
| FeI     | 4415.123  | 124.700 | 3.460              | 4.140     |
| FeI     | 4442.339  | 73.700  | 2.660              | 4.481     |
| FeI     | 4447.717  | 83.500  | 2.831              | 4.900     |
| FeI     | 4489.739  | 99.300  | 3.087              | 4.696     |
| FeI     | 4528.614  | 97.500  | 3.059              | 4.521     |
| FeI     | 4602.941  | 69.399  | 2.581              | 4.353     |
| FeI     | 4733.592  | 32.500  | 1.766              | 4.349     |
| FeI     | 4736.773  | 27.200  | 1.616              | 4.294     |
| FeI     | 4871.318  | 64.599  | 2.490              | 4.216     |
| FeI     | 4872.138  | 68.300  | 2.560              | 4.464     |
| FeI     | 4890.755  | 80.000  | 2.771              | 4.539     |
| FeI     | 4891.492  | 85.983  | 2.873              | 4.212     |
| FeI     | 4903.310  | 47.600  | 2.137              | 4.394     |

| Species | $\lambda$ | obs.eqw | error* | Abundance |
|---------|-----------|---------|--------|-----------|
| FeI     | 4918.994  | 82.600  | 2.816  | 4.543     |
| FeI     | 4920.502  | 99.200  | 3.086  | 4.563     |
| FeI     | 4939.687  | 68.560  | 2.565  | 4.425     |
| FeI     | 4994.130  | 95.200  | 3.023  | 4.709     |
| FeI     | 5001.864  | 34.500  | 1.820  | 4.478     |
| FeI     | 5014.943  | 18.900  | 1.347  | 4.499     |
| FeI     | 5049.820  | 73.900  | 2.663  | 4.559     |
| FeI     | 5051.635  | 106.799 | 3.202  | 4.689     |
| FeI     | 5068.766  | 33.000  | 1.780  | 4.277     |
| FeI     | 5079.740  | 69.700  | 2.586  | 4.504     |
| FeI     | 5083.339  | 89.400  | 2.929  | 4.586     |
| FeI     | 5123.720  | 64.100  | 2.480  | 4.332     |
| FeI     | 5127.359  | 69.361  | 2.580  | 4.447     |
| FeI     | 5142.928  | 79.200  | 2.757  | 4.544     |
| FeI     | 5150.840  | 74.400  | 2.672  | 4.350     |
| FeI     | 5166.282  | 89.600  | 2.932  | 4.306     |
| FeI     | 5171.596  | 99.900  | 3.096  | 4.107     |
| FeI     | 5192.344  | 78.394  | 2.743  | 4.607     |
| FeI     | 5194.942  | 104.700 | 3.170  | 4.806     |
| FeI     | 5216.274  | 85.100  | 2.858  | 4.588     |
| FeI     | 5225.526  | 47.600  | 2.137  | 4.425     |
| FeI     | 5232.940  | 92.300  | 2.976  | 4.439     |
| FeI     | 5247.050  | 36.700  | 1.877  | 4.372     |
| FeI     | 5250.209  | 49.400  | 2.177  | 4.593     |
| FeI     | 5250.646  | 39.300  | 1.942  | 4.562     |
| FeI     | 5266.555  | 61.700  | 2.433  | 4.287     |
| FeI     | 5270.356  | 148.900 | 3.780  | 4.794     |
| FeI     | 5283.621  | 49.100  | 2.171  | 4.375     |

| Species | $\lambda$ | obs.eqw | error* | Abundance |
|---------|-----------|---------|--------|-----------|
| FeI     | 5307.361  | 34.300  | 1.814  | 4.479     |
| FeI     | 5324.179  | 69.500  | 2.583  | 4.403     |
| FeI     | 5332.900  | 41.600  | 1.998  | 4.385     |
| FeI     | 5339.929  | 28.000  | 1.639  | 4.194     |
| FeI     | 5393.168  | 34.900  | 1.830  | 4.432     |
| FeI     | 5397.128  | 140.200 | 3.668  | 4.309     |
| FeI     | 5405.775  | 147.000 | 3.756  | 4.414     |
| FeI     | 5415.199  | 29.888  | 1.694  | 4.348     |
| FeI     | 5434.524  | 132.100 | 3.561  | 4.446     |
| FeI     | 5497.516  | 89.501  | 2.931  | 4.384     |
| FeI     | 5501.465  | 83.700  | 2.834  | 4.436     |
| FeI     | 5506.779  | 83.400  | 2.829  | 4.252     |
| FeI     | 5576.089  | 21.800  | 1.446  | 4.572     |
| FeI     | 5572.842  | 44.000  | 2.055  | 4.274     |
| FeI     | 5624.542  | 21.894  | 1.450  | 4.304     |
| FeI     | 6065.482  | 39.500  | 1.947  | 4.410     |
| FeI     | 6136.615  | 56.671  | 2.332  | 4.304     |
| FeI     | 6137.692  | 50.000  | 2.191  | 4.383     |
| FeI     | 6230.723  | 69.821  | 2.589  | 4.537     |
| FeI     | 6252.555  | 58.000  | 2.359  | 4.572     |
| FeI     | 6265.134  | 25.900  | 1.577  | 4.527     |
| FeI     | 6335.331  | 28.700  | 1.660  | 4.317     |
| FeI     | 6358.698  | 31.300  | 1.733  | 4.763     |
| FeI     | 6393.601  | 53.451  | 2.265  | 4.230     |
| FeI     | 6421.351  | 36.200  | 1.864  | 4.442     |
| FeI     | 6430.846  | 62.100  | 2.441  | 4.605     |

| Species | $\lambda$ | obs.eqw | error* | Abundance |
|---------|-----------|---------|--------|-----------|
| FeI     | 6494.980  | 78.500  | 2.745  | 4.429     |
| FeI     | 6592.914  | 40.400  | 1.969  | 4.434     |
| FeII    | 4233.172  | 94.400  | 3.010  | 5.001     |
| FeII    | 4491.405  | 17.600  | 1.300  | 4.136     |
| FeII    | 4583.837  | 68.400  | 2.562  | 4.458     |
| FeII    | 4923.921  | 106.100 | 3.191  | 4.993     |
| FeII    | 5018.440  | 103.600 | 3.153  | 4.776     |
| FeII    | 5197.568  | 33.800  | 1.801  | 13.002    |
| FeII    | 5316.615  | 77.600  | 2.729  | 4.910     |
| NiI     | 4855.406  | 8.100   | 0.882  | 3.040     |
| NiI     | 6643.629  | 11.300  | 1.041  | 2.946     |
| NiI     | 6767.768  | 16.200  | 1.247  | 3.165     |
| ZnI     | 4722.153  | 11.500  | 1.051  | 1.668     |
| ZnI     | 4810.528  | 9.300   | 0.945  | 1.434     |

\* The errors are computed using Cayrel's relation (Cayrel de Strobel & Spite 1988).

**Table 8**  
Linelist for SDSS J1341+4741

| Species | $\lambda$ | obs.eqw | error* | Abundance |
|---------|-----------|---------|--------|-----------|
| SiI     | 5268.387  | 4.600   | 0.664  | 5.457     |
| SiI     | 6237.319  | 4.200   | 0.635  | 5.358     |
| CaI     | 4226.728  | 112.700 | 3.289  | 3.221     |
| CaI     | 4283.011  | 10.300  | 0.994  | 3.401     |
| CaI     | 4302.528  | 23.800  | 1.511  | 3.368     |
| CaI     | 4318.652  | 18.700  | 1.340  | 3.710     |
| CaI     | 4425.437  | 27.400  | 1.622  | 3.910     |
| CaI     | 4454.779  | 39.600  | 1.950  | 3.558     |
| CaI     | 4585.865  | 12.200  | 1.082  | 3.679     |
| CaI     | 5857.451  | 9.100   | 0.935  | 3.834     |
| CaI     | 6122.217  | 28.700  | 1.660  | 3.959     |
| CaI     | 6162.173  | 32.700  | 1.772  | 3.841     |
| CaI     | 6439.075  | 21.600  | 1.440  | 3.677     |
| TiI     | 4533.241  | 15.600  | 1.224  | 2.419     |
| TiI     | 4981.731  | 13.100  | 1.121  | 2.288     |
| TiI     | 4991.065  | 6.000   | 0.759  | 2.036     |
| TiI     | 4999.503  | 9.800   | 0.970  | 2.368     |
| TiII    | 4012.385  | 17.500  | 1.296  | 1.789     |
| TiII    | 4028.343  | 21.100  | 1.423  | 2.522     |
| TiII    | 4163.648  | 3.200   | 0.554  | 1.598     |
| TiII    | 4171.910  | 3.500   | 0.580  | 1.739     |
| TiII    | 4290.219  | 49.800  | 2.186  | 2.259     |
| TiII    | 4300.049  | 53.300  | 2.262  | 1.899     |
| TiII    | 4312.864  | 22.400  | 1.466  | 1.933     |
| TiII    | 4395.033  | 58.600  | 2.372  | 1.888     |
| TiII    | 4443.794  | 52.200  | 2.238  | 1.965     |

| Species | $\lambda$ | obs.eqw | error* | Abundance |
|---------|-----------|---------|--------|-----------|
| TiII    | 4468.507  | 57.900  | 2.357  | 2.013     |
| TiII    | 4501.273  | 48.400  | 2.155  | 1.974     |
| TiII    | 4533.969  | 49.800  | 2.186  | 1.904     |
| TiII    | 4563.761  | 36.600  | 1.874  | 1.887     |
| TiII    | 4571.968  | 31.800  | 1.747  | 1.599     |
| CrI     | 4254.332  | 54.600  | 2.289  | 2.187     |
| CrI     | 4274.796  | 59.800  | 2.396  | 2.377     |
| CrI     | 4289.716  | 46.200  | 2.106  | 2.240     |
| CrI     | 5204.506  | 14.600  | 1.184  | 2.296     |
| CrI     | 5206.038  | 31.900  | 1.750  | 2.504     |
| CrI     | 5208.419  | 39.100  | 1.937  | 2.509     |
| CrI     | 4824.127  | 4.300   | 0.642  | 2.834     |
| MnI     | 3823.507  | 37.100  | 1.887  | 3.290     |
| MnI     | 4030.753  | 41.100  | 1.986  | 1.622     |
| MnI     | 4033.062  | 15.200  | 1.208  | 1.178     |
| MnI     | 4034.483  | 17.900  | 1.311  | 1.449     |
| MnI     | 4823.524  | 3.800   | 0.604  | 2.165     |
| FeI     | 4005.242  | 72.350  | 2.635  | 4.325     |
| FeI     | 4045.812  | 109.200 | 3.237  | 4.339     |
| FeI     | 4132.058  | 73.770  | 2.661  | 4.379     |
| FeI     | 4143.868  | 77.740  | 2.732  | 4.299     |
| FeI     | 4187.039  | 41.910  | 2.006  | 4.452     |
| FeI     | 4187.795  | 36.600  | 1.874  | 4.310     |
| FeI     | 4198.304  | 29.080  | 1.671  | 4.306     |
| FeI     | 4202.029  | 73.499  | 2.656  | 4.140     |
| FeI     | 4227.427  | 19.970  | 1.384  | 3.934     |
| FeI     | 4250.119  | 31.760  | 1.746  | 4.095     |

| Species | $\lambda$ | obs.eqw | error* | Abundance |
|---------|-----------|---------|--------|-----------|
| FeI     | 4250.787  | 66.470  | 2.526  | 4.165     |
| FeI     | 4260.474  | 63.579  | 2.470  | 4.213     |
| FeI     | 4271.154  | 47.860  | 2.143  | 4.437     |
| FeI     | 4271.760  | 92.450  | 2.979  | 3.977     |
| FeI     | 4325.762  | 83.979  | 2.839  | 3.897     |
| FeI     | 4375.930  | 41.550  | 1.997  | 4.511     |
| FeI     | 4383.545  | 112.400 | 3.284  | 4.508     |
| FeI     | 4404.750  | 86.770  | 2.886  | 4.355     |
| FeI     | 4415.122  | 69.280  | 2.579  | 4.522     |
| FeI     | 4427.310  | 31.930  | 1.751  | 4.399     |
| FeI     | 4528.614  | 38.710  | 1.927  | 4.440     |
| FeI     | 4531.148  | 21.030  | 1.421  | 4.644     |
| FeI     | 4583.721  | 25.720  | 1.571  | 7.103     |
| FeI     | 4871.318  | 28.190  | 1.645  | 4.433     |
| FeI     | 4872.138  | 26.150  | 1.584  | 4.603     |
| FeI     | 4891.492  | 40.500  | 1.972  | 4.401     |
| FeI     | 4918.994  | 26.150  | 1.584  | 4.360     |
| FeI     | 5006.119  | 16.280  | 1.250  | 4.348     |
| FeI     | 5041.756  | 13.310  | 1.130  | 4.420     |
| FeI     | 5171.596  | 26.600  | 1.598  | 4.370     |
| FeI     | 5194.942  | 20.500  | 1.403  | 4.603     |
| FeI     | 5216.274  | 11.600  | 1.055  | 4.429     |
| FeI     | 5232.940  | 38.020  | 1.910  | 4.387     |
| FeI     | 5266.555  | 19.990  | 1.385  | 4.388     |
| FeI     | 5269.537  | 76.789  | 2.715  | 4.240     |
| FeI     | 5324.179  | 27.990  | 1.639  | 4.632     |
| FeI     | 5328.039  | 79.800  | 2.767  | 4.483     |
| FeI     | 5328.532  | 22.770  | 1.478  | 4.404     |

| Species | $\lambda$ | obs.eqw | error* | Abundance |
|---------|-----------|---------|--------|-----------|
| FeI     | 5371.490  | 67.410  | 2.544  | 4.445     |
| FeI     | 5397.128  | 55.110  | 2.300  | 4.490     |
| FeI     | 5405.775  | 58.820  | 2.376  | 4.487     |
| FeI     | 5429.697  | 57.280  | 2.345  | 4.474     |
| FeI     | 5434.524  | 36.540  | 1.873  | 4.386     |
| FeI     | 5446.917  | 56.490  | 2.328  | 4.522     |
| FeI     | 5455.609  | 45.910  | 2.099  | 4.532     |
| FeI     | 5572.842  | 12.470  | 1.094  | 4.478     |
| FeI     | 5615.644  | 24.400  | 1.530  | 4.603     |
| FeI     | 6230.723  | 16.000  | 1.239  | 4.670     |
| FeI     | 6494.980  | 18.970  | 1.349  | 4.552     |
| FeII    | 4233.172  | 30.390  | 1.708  | 4.243     |
| FeII    | 4508.288  | 15.630  | 1.225  | 4.494     |
| FeII    | 4515.339  | 5.290   | 0.713  | 4.132     |
| FeII    | 4522.634  | 7.240   | 0.834  | 3.890     |
| FeII    | 4555.893  | 2.260   | 0.466  | 3.527     |
| FeII    | 4583.837  | 25.720  | 1.571  | 4.294     |
| FeII    | 4923.927  | 48.280  | 2.153  | 4.255     |
| CoI     | 4092.384  | 7.900   | 0.871  | 2.267     |
| CoI     | 4121.311  | 11.400  | 1.046  | 1.823     |
| NiI     | 3807.138  | 30.300  | 1.705  | 2.603     |
| NiI     | 4401.538  | 7.000   | 0.820  | 3.374     |
| NiI     | 4459.027  | 22.000  | 1.453  | 4.258     |
| NiI     | 5476.900  | 20.600  | 1.406  | 3.348     |

\* The errors are computed using Cayrel's relation (Cayrel de Strobel & Spite 1988) .

## REFERENCES

- Alonso, A., Arribas, S., & Martínez-Roger, C. 1996, *A&A*, 313, 873
- Alonso, A., Arribas, S., & Martínez-Roger, C. 1999, *A&AS*, 140, 261
- Alvarez, R., & Plez, B. 1998, *A&A*, 330, 1109
- Anders, F., et al. 2014, *A&A*, 564, A115
- Aoki, W., Beers, T. C., Christlieb, N., Norris, J. E., Ryan, S. G., & Tsangarides, S. 2007, *ApJ*, 655, 492
- Aoki, W., et al. 2013, *AJ*, 145, 13
- Argast, D., Samland, M., Thielemann, F.-K., & Qian, Y.-Z. 2004, *A&A*, 416, 997
- Arnett, W. D. 1971, *ApJ*, 166, 153
- Asplund, M. 2005, *Highlights of Astronomy*, 13, 542
- Asplund, M., Grevesse, N., Sauval, A. J., & Scott, P. 2009, *ARA&A*, 47, 481
- Audouze, J., & Silk, J. 1995, *ApJL*, 451, L49
- Baumüller, D., & Gehren, T. 1997, *A&A*, 325, 1088
- Bayo, A., Rodrigo, C., Barrado Y Navascués, D., Solano, E., Gutiérrez, R., Morales-Calderón, M., & Allard, F. 2008, *A&A*, 492, 277
- Beers, T. C., & Christlieb, N. 2005, *ARA&A*, 43, 531
- Beers, T. C., Preston, G. W., & Smetman, S. A. 1985, *AJ*, 90, 2089
- . 1992, *AJ*, 103, 1987
- Beers, T. C., et al. 2017, *ApJ*, 835, 81
- Bergemann, M., & Cescutti, G. 2010, *A&A*, 522, A9
- Bonifacio, P., et al. 2007, *A&A*, 462, 851
- . 2009, *A&A*, 501, 519
- . 2015, *A&A*, 579, A28
- Bromm, V., Yoshida, N., Hernquist, L., & McKee, C. F. 2009, *Nature*, 459, 49
- Cameron, A. G. W., & Fowler, W. A. 1971, *ApJ*, 164, 111
- Carretta, E., Bragaglia, A., D'Orazi, V., Lucatello, S., & Gratton, R. G. 2010, *A&A*, 519, A71
- Carretta, E., Gratton, R., Cohen, J. G., Beers, T. C., & Christlieb, N. 2002, *AJ*, 124, 481
- Castelli, F., & Kurucz, R. L. 2004, *ArXiv Astrophysics e-prints*
- Cayrel, R., et al. 2004, *A&A*, 416, 1117
- Cayrel de Strobel, G., & Spite, M., eds. 1988, *IAU Symposium*, Vol. 132, The impact of very high S/N spectroscopy on stellar physics: proceedings of the 132nd Symposium of the International Astronomical Union held in Paris, France, June 29-July 3, 1987.
- Chiaki, G., Susa, H., & Hirano, S. 2018, *MNRAS*, 475, 4378
- Chiaki, G., Tominaga, N., & Nozawa, T. 2017, *MNRAS*, 472, L115
- Chiappini, C. 2013, *Astronomische Nachrichten*, 334, 595
- Choplin, A., Maeder, A., Meynet, G., & Chiappini, C. 2016, *A&A*, 593, A36
- Christlieb, N. 2003, in *Reviews in Modern Astronomy*, Vol. 16, *Reviews in Modern Astronomy*, ed. R. E. Schielicke, 191
- Coelho, P., Percival, S. M., & Salaris, M. 2011, *ApJ*, 734, 72
- Cooke, R. J., & Madau, P. 2014, *The Astrophysical Journal*, 791, 116
- Cowan, J. J., & Rose, W. K. 1977, *ApJ*, 212, 149
- de Laverny, P., Recio-Blanco, A., Worley, C. C., & Plez, B. 2012, *A&A*, 544, A126
- Denissenkov, P. A., & Herwig, F. 2004, *ApJ*, 612, 1081
- Drout, M. R., et al. 2017, *Science*, 358, 1570
- Eisenstein, D. J., et al. 2011, *AJ*, 142, 72
- Fernández-Alvar, E., Allende Prieto, C., Beers, T. C., Lee, Y. S., Masseron, T., & Schneider, D. P. 2016, *A&A*, 593, A28
- Frebel, A., & Norris, J. E. 2015, *ARA&A*, 53, 631
- Frebel, A., et al. 2006, *ApJ*, 652, 1585
- Fulbright, J. P., et al. 2010, *ApJL*, 724, L104
- García Pérez, A. E., et al. 2013, *ApJL*, 767, L9
- Gratton, R., Sneden, C., & Carretta, E. 2004, *ARA&A*, 42, 385
- Gratton, R. G., et al. 2001, *A&A*, 369, 87
- Grevesse, N., Scott, P., Asplund, M., & Sauval, A. J. 2015, *A&A*, 573, A27
- Gustafsson, B., Edvardsson, B., Eriksson, K., Jørgensen, U. G., Nordlund, Å., & Plez, B. 2008, *A&A*, 486, 951
- Hempel, M., Stancliffe, R. J., Lugaro, M., & Meyer, B. S. 2016, *ApJ*, 831, 171
- Hansen, T. T., Andersen, J., Nordström, B., Beers, T. C., Placco, V. M., Yoon, J., & Buchhave, L. A. 2016a, *A&A*, 586, A160
- . 2016b, *A&A*, 588, A3
- Heger, A., & Woosley, S. E. 2002, *ApJ*, 567, 532
- . 2010, *ApJ*, 724, 341
- Ivezić, Ž., Beers, T. C., & Jurić, M. 2012, *ARA&A*, 50, 251
- Johnson, J. A., Herwig, F., Beers, T. C., & Christlieb, N. 2007, *ApJ*, 658, 1203
- Kilpatrick, C. D., et al. 2017, *Science*, 358, 1583
- Lai, D. K., Bolte, M., Johnson, J. A., Lucatello, S., Heger, A., & Woosley, S. E. 2008, *ApJ*, 681, 1524
- Lau, H. H. B., Stancliffe, R. J., & Tout, C. A. 2007, *MNRAS*, 378, 563
- Lee, Y. S., Beers, T. C., Kim, Y. K., Placco, V., Yoon, J., Carollo, D., Masseron, T., & Jung, J. 2017, *ApJ*, 836, 91
- Lee, Y. S., et al. 2013, *AJ*, 146, 132
- Li, H.-N., Zhao, G., Christlieb, N., Wang, L., Wang, W., Zhang, Y., Hou, Y., & Yuan, H. 2015, *ApJ*, 798, 110
- Lucatello, S., Tsangarides, S., Beers, T. C., Carretta, E., Gratton, R. G., & Ryan, S. G. 2005, *The Astrophysical Journal*, 625, 825
- Maeder, A., & Meynet, G. 2015, *A&A*, 580, A32
- Maeder, A., Meynet, G., & Chiappini, C. 2015, *A&A*, 576, A56
- Masseron, T., Johnson, J. A., Lucatello, S., Karakas, A., Plez, B., Beers, T. C., & Christlieb, N. 2012, *ApJ*, 751, 14
- Masseron, T., et al. 2006, *A&A*, 455, 1059
- Matsuno, T., Aoki, W., Beers, T. C., Lee, Y. S., & Honda, S. 2017, *AJ*, 154, 52
- McWilliam, A. 1998, *AJ*, 115, 1640
- McWilliam, A., Preston, G. W., Sneden, C., & Searle, L. 1995, *AJ*, 109, 2757
- Mészáros, S., et al. 2015, *AJ*, 149, 153
- Meynet, G., Ekström, S., & Maeder, A. 2006, *A&A*, 447, 623
- Meynet, G., Hirschi, R., Ekström, S., Maeder, A., Georgy, C., Eggenberger, P., & Chiappini, C. 2010, *A&A*, 521, A30
- Nakamura, T., Umeda, H., Nomoto, K., Thielemann, F.-K., & Burrows, A. 1999, *ApJ*, 517, 193
- Nishimura, N., Takiwaki, T., & Thielemann, F.-K. 2015, *ApJ*, 810, 109
- Nomoto, K., Kobayashi, C., & Tominaga, N. 2013, *ARA&A*, 51, 457
- Paegert, M., et al. 2015, *AJ*, 149, 186
- Peterson, R. C. 1976, *ApJ*, 206, 800
- Piau, L., Beers, T. C., Balsara, D. S., Sivarani, T., Truran, J. W., & Ferguson, J. W. 2006, *ApJ*, 653, 300
- Pinsonneault, M. H., Walker, T. P., Steigman, G., & Narayanan, V. K. 1999, *ApJ*, 527, 180
- Placco, V. M., et al. 2016, *ApJ*, 833, 21
- Plez, B., & Cohen, J. G. 2005, *A&A*, 434, 1117
- Pols, O. R., Izzard, R. G., Glebbeek, E., & Stancliffe, R. J. 2009, *PASA*, 26, 327
- Pols, O. R., Izzard, R. G., Stancliffe, R. J., & Glebbeek, E. 2012, *A&A*, 547, A76
- Qian, Y.-Z., & Wasserburg, G. J. 2002, *ApJ*, 567, 515
- Ramírez, I., & Meléndez, J. 2005, *ApJ*, 626, 465
- Ryan, S. G., Norris, J. E., & Beers, T. C. 1996, *ApJ*, 471, 254
- Scott, P., Asplund, M., Grevesse, N., Bergemann, M., & Sauval, A. J. 2015a, *A&A*, 573, A26
- Scott, P., et al. 2015b, *A&A*, 573, A25
- Shappee, B. J., et al. 2017, *Science*, 358, 1574
- Sharma, M., Theuns, T., Frenk, C. S., & Cooke, R. J. 2018, *MNRAS*, 473, 984
- Shetrone, M. D. 1996, in *Astronomical Society of the Pacific Conference Series*, Vol. 92, *Formation of the Galactic Halo...Inside and Out*, ed. H. L. Morrison & A. Sarajedini, 383
- Shi, J. R., Takada-Hidai, M., Takeda, Y., Tan, K. F., Hu, S. M., Zhao, G., & Cao, C. 2012, *ApJ*, 755, 36
- Sivarani, T., et al. 2006, *A&A*, 459, 125
- Smith, B. D., Wise, J. H., O'Shea, B. W., Norman, M. L., & Khochfar, S. 2015, *MNRAS*, 452, 2822
- Spite, F., & Spite, M. 1982, *A&A*, 115, 357
- Spite, M., Caffau, E., Bonifacio, P., Spite, F., Ludwig, H.-G., Plez, B., & Christlieb, N. 2013, *A&A*, 552, A107
- Spite, M., et al. 2005, *A&A*, 430, 655
- . 2006, *A&A*, 455, 291
- Starkenburg, E., Shetrone, M. D., McConnachie, A. W., & Venn, K. A. 2014, *MNRAS*, 441, 1217
- Steigman, G. 2005, *Physica Scripta Volume T*, 121, 142
- Suda, T., et al. 2008, *PASJ*, 60, 1159
- Suda, T., et al. 2012, *AGB evolution and nucleosynthesis at low-metallicity constrained by the star formation history of our galaxy*, ed. J. Lattanzio, A. Karakas, & G. Dracoulis (Scuola Internazionale Superiore di Studi Avanzati (S I S S A)), 1 – 5
- Susmitha Rani, A., Sivarani, T., Beers, T. C., Fleming, S., Mahadevan, S., & Ge, J. 2016, *MNRAS*, 458, 2648
- Tominaga, N., Iwamoto, N., & Nomoto, K. 2014, *ApJ*, 785, 98
- Truran, J. W., & Arnett, W. D. 1971, *Ap&SS*, 11, 430
- Umeda, H., & Nomoto, K. 2003, *Nature*, 422, 871
- . 2005, *ApJ*, 619, 427
- Umeda, H., Nomoto, K., & Nakamura, T. 2000, in *The First Stars*, ed. A. Weiss, T. G. Abel, & V. Hill, 150

- Winteler, C., Käppeli, R., Perego, A., Arcones, A., Vasset, N., Nishimura, N., Liebendörfer, M., & Thielemann, F.-K. 2012, *ApJL*, 750, L22
- Woosley, S. E., & Weaver, T. A. 1986, *ARA&A*, 24, 205
- Wright, J. T., & Howard, A. W. 2009, *ApJS*, 182, 205
- Yoon, J., et al. 2016, *ApJ*, 833, 20
- Zhao, G., Zhao, Y., Chu, Y., Jing, Y., & Deng, L. 2012, *ArXiv e-prints*